Exoplanet Statistics and Theoretical Implications

Wei Zhu[1,2] and Subo Dong[3,*]

[1]Department of Astronomy, Tsinghua University, Beijing, China, Beijing 100084; email: weizhu@tsinghua.edu.cn
[2]Canadian Institute for Theoretical Astrophysics, University of Toronto, Toronto, Canada, ON M5S 3H8
[3]Kavli Institute for Astronomy and Astrophysics, Peking University, Beijing, China, Beijing 100871; email: dongsubo@pku.edu.cn

Xxxx. Xxx. Xxx. Xxx. YYYY. AA:1–49

https://doi.org/10.1146/((please add article doi))

Keywords

exoplanets, planetary systems, orbital properties, planet formation, dynamical evolution

Abstract

In the last few years, significant advances have been made in understanding the distributions of exoplanet populations and the architecture of planetary systems. We review the recent progress of planet statistics, with a focus on the inner $\lesssim 1\,\mathrm{AU}$ region of the planetary system that has been fairly thoroughly surveyed by the *Kepler* mission. We also discuss the theoretical implications of these statistical results for planet formation and dynamical evolution.

*Corresponding author

Contents

1. INTRODUCTION

"Who ordered that?" said the theorist I. Rabi when learning about the unexpected discovery of muons in 1936. Little did particle physicists know that it would only be the beginning of uncovering a puzzling "particle zoo" filled with diverse particles in the next three decades, until revolutionary theoretical insights were developed to classify the elementary particles. Now nearly three decades since the astonishing discovery of a hot Jupiter (Mayor & Queloz 1995), the "exoplanet zoo" is ever growing – whenever the detection territories grow in breadth or depth, nature appears to be teeming with new species. Theorists working on planet formation and evolution face distinctly different sets of challenges from particle physicists: in the popular paradigm, forming planets from dust grains is a daunting march spanning tens of orders of magnitudes in mass and involves many physical processes that are too complex for first-principle calculations. In hindsight, it should probably be of little surprise that a theory involving such complicated physics, which was anchored by the sole sample of our solar system, would have limited predictive success.

We review the recent progress of planet statistics and identify patterns emerging from the known thousands of exoplanets that cover a broad region of the parameter space (see **Figure 1**). Robustly identifying patterns in the intrinsic distributions of planets can stimulate and test theories. Conversely, theoretical advances may also beam the searchlight on fresh observational ground, as exemplified by the development of the photoevaporation theory leading to the recent discovery of a "radius valley" (see Section 2.1.4). Since the last *Annual Reviews* article on exoplanet populations (Winn & Fabrycky 2015), the field of planet statistics has made significant progress. In particular, the large and homogeneous planet sample from the NASA *Kepler* mission (Borucki et al. 2010) has provided the best source for statistical studies, but a major shortcoming of the *Kepler* data was the initial lack of accurate stellar parameters for both the planet hosts and the target stars (i.e., the parent

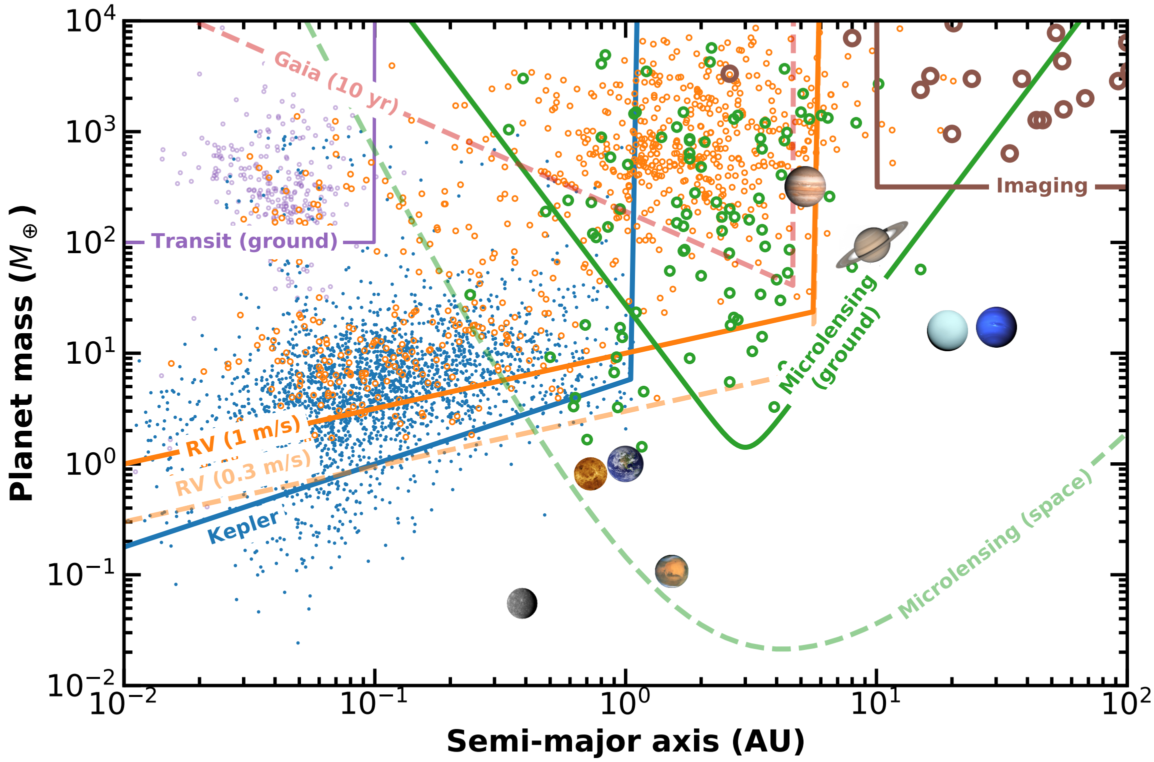


Figure 1

Mass versus semi-major axis of known planets, based on the "Confirmed Planets" list from NASA Exoplanet Archive (Akeson et al. 2013, acquired in September of 2020) and the reliable *Kepler* planet candidates (see Section 2 for more details). We differentiate with different colors planet detections as well as the approximate sensitivity curves from ground-based transit (purple), *Kepler* survey (blue), RV surveys (orange), microlensing (green), and direct imaging (brown). The masses of the *Kepler* detections are estimated from the measured radii according to the Chen & Kipping (2017) mass–radius relation. The sensitivity curve of *Kepler* is also converted in a similar way from that measured in the radius–period plane (see **Figure 2**). The sensitivity curve for the 10-yr *Gaia* astrometry survey is also shown in red, for which we have assumed a Sun-like host at 20 pc and required a 3-σ detection over the expected precision. For space-based microlensing, we adopt the sensitivity curve of the microlensing survey that will be performed by the *Nancy Grace Roman Space Telescope* (formerly known as WFIRST, Penny et al. 2019). Images of the solar system planets from NASA are shown at their corresponding locations.

sample). In the last few years, substantial efforts have been dedicated to systematically characterize the *Kepler* sample and thus unleash its potential for statistical studies. These include asteroseismology (e.g., Chaplin & Miglio 2013, Van Eylen & Albrecht 2015), the *Gaia* data releases (Gaia Collaboration et al. 2016, 2018), follow-up spectroscopic programs such as the LAMOST-*Kepler* survey (e.g., Dong et al. 2014b, De Cat et al. 2015, Zong et al. 2018) and the California-*Kepler* Survey (CKS, Petigura et al. 2017, Johnson et al. 2017), as well as many projects of the *Kepler* Follow-up Observation Program (KFOP, Furlan et al. 2017). Moreover, substantial works to understand the *Kepler* pipeline detection efficiency and vetting false positives have much improved the reliability of *Kepler* statistical

inference (e.g., Christiansen et al. 2015, Morton et al. 2016). Last but not least, in-depth developments have been recently made to disentangle the intricate observational biases of multi-planet systems. These efforts have made it possible to offer new insights into planet distributions and architectures.

In this review, we first clarify in Sections 1.1 and 1.2 several common confusions in exoplanet statistical studies. Then we discuss planet distributions in the inner ($\lesssim 1\,\mathrm{AU}$) and the outer (~ 1–$10\,\mathrm{AU}$) regions in Sections 2 and 3, respectively. The former is focused on results from the *Kepler* mission, and the latter includes updated results from radial velocity (RV) and gravitational microlensing. A brief discussion of the free-floating planets (FFPs) from microlensing is also provided. We focus on planets around $\gtrsim$Gyr-old stars, while planets orbiting young stars found by direct imaging are not discussed (see the review by Bowler 2016). The implications to theories of planet formation and evolution are discussed in Section 4. Finally in Section 5, we summarize and outline the promising directions for future developments.

1.1. On defining and interpreting planet "occurrence rate"

Many statistical studies focus on deriving the intrinsic "occurrence rate" (or the often interchangeably used term "frequency") of planets. But from one study to another, the same term can carry different meanings. In the following we clarify these different definitions to avoid further misinterpretations.

In most studies, the derived occurrence rate is the average number of planets per star, and we denote it as $\bar{n}_\mathrm{p}$, which is defined as

$$\bar{n}_\mathrm{p} \equiv \frac{\text{Total \# of planets}}{\text{Total \# of stars}}. \qquad 1.$$

Frequency of planets: the average number of planets per star $\bar{n}_\mathrm{p}$ (Equation 1).

Frequency of planetary systems: the fraction of stars with planets F_p (Equation 2).

Average planet multiplicity: the average number of planets per planetary system (Equation 3).

Here *a planet* is restricted to lie within a predefined parameter space, often in the period–radius plane (for the transit method) or the period–mass (or minimum mass $m_\mathrm{p}\sin i$) plane (for the RV method). Similarly, *a star* is restricted to a star-like target of predefined properties. Since a large fraction of such stars may actually have unresolved stellar companions, the correction for the impact of the stellar binarity can be important for the inference of the planet formation efficiency (see Section 2.5.1).

Another important quantity sometimes referred to as occurrence rate is the fraction of stars with planets F_p

$$F_\mathrm{p} \equiv \frac{\text{Total \# of planetary systems}}{\text{Total \# of stars}}. \qquad 2.$$

Here a planetary system has *at least one* planet existing in a predefined parameter space. By definition $F_\mathrm{p} \leq 1$, so it is usually reported as a percentage. However, an occurrence rate reported as a percentage (i.e., "X% of stars have planets") does not necessarily mean that it is the fraction of stars that are hosts of planets, since $\bar{n}_\mathrm{p}$ is also frequently reported as a percentage.

To distinguish between the two definitions, we refer to $\bar{n}_\mathrm{p}$ as the frequency of planets and F_p as the frequency of planetary systems. The ratio of the two measures the average number of planets per planetary system (within a predefined parameter space), which we call *average planet multiplicity* and denote $\bar{m}_\mathrm{p}$

$$\bar{m}_\mathrm{p} \equiv \frac{\bar{n}_\mathrm{p}}{F_\mathrm{p}} = \frac{\text{Total \# of planets}}{\text{Total \# of planetary systems}}. \qquad 3.$$

Kepler data suggest that multi-planet systems are common, so usually $\bar{m}_{\rm p}$ is larger than unity, and consequently $\bar{n}_{\rm p}$ and $F_{\rm p}$ substantially differ from each other. They only become similar when the average planet multiplicity $\bar{m}_{\rm p} \rightarrow 1$, which can happen when either a) a category of planets with low intrinsic multiplicity (e.g., short-period giant planets) is concerned, or b) the parameter space of interest is small enough that systems with more than one such planet are rare.

The three quantities, $\bar{n}_{\rm p}$, $F_{\rm p}$, and $\bar{m}_{\rm p}$, are all important for testing theories. To provide a simple example, with only $\bar{n}_{\rm p}$ measured to be unity, it is possible that all stars have one planet ($F_{\rm p} = 100\%$ and $\bar{m}_{\rm p} = 1$) or that half of the stars have two planets ($F_{\rm p} = 50\%$ and $\bar{m}_{\rm p} = 2$). These two cases obviously demand different theoretical explanations.

Observationally, the derivations of $\bar{n}_{\rm p}$ and $F_{\rm p}$ have rather different requirements and follow different procedures. It is generally more straightforward to derive $\bar{n}_{\rm p}$, since correcting the detectability of individual planets concerns observables directly measurable from surveys (e.g., planet size and orbital period for transit, assuming that the properties of the stars are known). In contrast, the detectability of a planetary system usually concerns the intrinsic architecture of the system, including the planet multiplicity and distributions of the orbital and physical parameters, many of which may not be directly observable, so the derivation of $F_{\rm p}$ can rely on assumptions of these unknowns. This is especially an issue in transit surveys: the derivation of $F_{\rm p}$ requires assumptions about the mutual inclinations between planets, and different assumptions can lead to fairly different values of $F_{\rm p}$ (see Section 2.2).

In deriving the two frequencies, statistical studies involving multi-planet systems usually treat the planet occurrence as a Poisson process. This may be a reasonable assumption in the derivation of the planet frequency $\bar{n}_{\rm p}$, but it can lead to unreliable results in the derivation of the planetary system frequency $F_{\rm p}$. This Poisson process assumption implies that the presences of individual planets in the same system are independent and that their physical and orbital properties are independent of the properties of other planets or of the host star. As discussed later in this review, such an assumption breaks down in certain circumstances. Below we provide a specific example to demonstrate its impact on the planetary system frequency. The fractions of Sun-like stars with cold giant planets and with planets that *Kepler* is sensitive to are 10% and 30%, respectively. The fraction of such stars with at least one planet in the joint parameter space would be $1-(1-30\%)\times(1-10\%) = 37\%$ under the Poisson process assumption. However, this frequency is determined to be $\sim 30\%$ as a result of the strong correlation between the inner and the outer planets (Section 3.2). The correlations (or sometimes anti-correlations) between the occurrences of planets around the same host also suggest that one may not be able to extrapolate a parameterized distribution of the planetary system frequency to a parameter space that is not covered by the data.

A number of studies have reported $F_{\rm p}$ by using the detectability of the first detected (or the most detectable) planet in the system as that of the whole system (e.g., Cumming et al. 2008, Mayor et al. 2011, Fressin et al. 2013, Petigura et al. 2013). This approach does not require assumptions on planet multiplicity or architecture. However, as the detectability of any planet is no greater than the detectability of the system it resides in, this approach typically tends to overestimate $F_{\rm p}$ (Zhu et al. 2018b).

1.2. On inferring the frequency of planets

In this section, we discuss the commonly used methods of inferring the frequency of planets $\bar{n}_\mathrm{p}$ from a statistical survey of $N_\star$ target stars.

A popular method is the so-called inverse detection efficiency method (IDEM), which has been used extensively in the literature, including many influential studies (e.g., Mayor et al. 2011, Howard et al. 2012, Fressin et al. 2013, Petigura et al. 2013, Dressing & Charbonneau 2013, 2015). For our illustrative survey, the average number of planets per star according to IDEM is

$$\bar{n}_\mathrm{p}^\mathrm{IDEM} = \frac{1}{N_\star} \sum_{i=1}^{N_\mathrm{p}} \frac{1}{p_i} = \frac{N_\mathrm{p}}{N_\star} \left\langle \frac{1}{p} \right\rangle \ . \qquad 4.$$

Here p_i is the survey detection efficiency of the i-th of N_p detected planets and $\langle \cdot \rangle$ is the average over all detected planets. IDEM is intuitive, simple to perform, and computationally efficient, as it does not require computing the detection efficiencies of null detections (which are usually the majority of the targets), so it is useful in getting a rough estimate of the underlying frequency. However, this method is not rigorously established in the probability theory and can potentially lead to biased results (Foreman-Mackey et al. 2014, Hsu et al. 2018). Specifically, with a low detection efficiency and a small number of detections, Hsu et al. (2018) found that IDEM often leads to underestimated $\bar{n}_\mathrm{p}$ since the actual detections typically come from targets with larger-than-average sensitivities. IDEM can also suffer substantial fluctuations because of the inversion of the (typically small) detection efficiency.

An approach with sound statistical basis is modeling planet occurrence as a Poisson process and performing maximum likelihood analysis (e.g., Tabachnik & Tremaine 2002, Cumming et al. 2008, Gould et al. 2010, Youdin 2011, Dong & Zhu 2013, Burke et al. 2015). In a given bin that has N_p planet detections, Youdin (2011, see their Section 3.1) and Foreman-Mackey et al. (2014, see their Appendix A) show that the maximum likelihood (ML) estimator for planet frequency is

$$\bar{n}_\mathrm{p}^\mathrm{ML} = \frac{N_\mathrm{p}}{\sum_{j=1}^{N_\star} p_j} = \frac{N_\mathrm{p}}{N_\star} \frac{1}{\langle p \rangle} = \frac{N_\mathrm{p}}{N_\star^\mathrm{eff}} \ ; \quad N_\star^\mathrm{eff} \equiv N_\star \langle p \rangle \ . \qquad 5.$$

Here p_j is the planetary detection efficiency in the bin for the j-th star, regardless of whether the star yields any actual planet detection or not, and $N_\star^\mathrm{eff}$ is the effective sample size. Unlike in **Equation (4), the average here is performed among all stars in the sample.** Compared to IDEM, this method is computationally more expensive, while being statistically superior. It is more robust against fluctuations in the efficiencies of individual detections (as well as null detections) because the averaging is performed on p rather than $1/p$.

Next we elaborate on incorporating the above approach into the Bayesian framework following the simplified Bayesian model of Hsu et al. (2018, see their Appendix B) but with some corrections. The posterior probability distribution of planet frequency $\bar{n}_\mathrm{p}$ for the statistical sample is given by

$$P(\bar{n}_\mathrm{p} | N_\mathrm{p},\ N_\star^\mathrm{eff}) \propto P(N_\mathrm{p} | \bar{n}_\mathrm{p},\ N_\star^\mathrm{eff}) P_\mathrm{pri}(\bar{n}_\mathrm{p}). \qquad 6.$$

The first term on the right-hand side quantifies the probability (or likelihood) of having the N_p detections for a given rate $\bar{n}_\mathrm{p}$, which under the Poisson process assumption is described

by a Gamma distribution [1]. The second term, $P_{\rm pri}(\bar{n}_{\rm p})$, is the prior distribution of $\bar{n}_{\rm p}$. If a conjugate prior is assigned as a Gamma distribution with a shape parameter α_0 and a rate parameter β_0, the resulting posterior distribution is then a Gamma distribution with the shape parameter $\alpha_0 + N_{\rm p}$ and the rate parameter $\beta_0 + N_\star^{\rm eff}$

$$P(\bar{n}_{\rm p}|N_{\rm p},\ N_\star^{\rm eff}) \propto \bar{n}_{\rm p}^{\alpha_0+N_{\rm p}-1} e^{-\bar{n}_{\rm p}(\beta_0+N_\star^{\rm eff})}. \qquad 7.$$

For a flat prior on $\bar{n}_{\rm p}$, the two parameters are $\alpha_0 = 1$ and $\beta_0 = 0$, respectively. For completeness, the mean and standard deviation of this Gamma distribution posterior are

$$\mu(\bar{n}_{\rm p}) = \frac{\alpha_0 + N_{\rm p}}{\beta_0 + N_\star^{\rm eff}}, \quad \sigma(\bar{n}_{\rm p}) = \frac{\sqrt{\alpha_0 + N_{\rm p}}}{\beta_0 + N_\star^{\rm eff}}. \qquad 8.$$

The first expression reduces to the ML estimator of **Equation 5** if a log-flat prior on the planet frequency $\bar{n}_{\rm p}$ is assumed (i.e., $\alpha_0 = \beta_0 = 0$). The expressions given by **Equation 8** provide easy-to-use estimates to report when the number of detections is relatively large. However, when small or null detections are involved, the posterior probability distribution is fairly non-Gaussian. It is then more appropriate to report the median value, the 68% credible interval, and/or the 95% upper limit, all of which can be derived from the cumulative posterior probability distribution. It is also worth noting that, in the case of null detections, a meaningful upper limit on $\bar{n}_{\rm p}$ cannot be derived with the log-flat prior because the shape parameter becomes zero and the Gamma distribution is undefined. We show in Section 2.1 an application of the Bayesian approach to derive the frequency of planets in the *Kepler* parameter space.

2. THE INNER PLANETARY SYSTEM

We review in this section planet statistics in the inner region ($\lesssim 1$ AU of Sun-like stars), which is well explored thanks to thousands of planets detected by the RV and transit techniques. We focus on the best statistical probe by far of the inner region—the large and uniform sample from the *Kepler* mission, which is sensitive to transiting planets with radii $R_{\rm p}$ down to $\sim R_\oplus$ and orbital periods P up to ~ 1 yr (Borucki et al. 2010).

We first derive a clean baseline sample based on the final *Kepler* data release (DR25, Thompson et al. 2018) and the improved stellar parameters from Berger et al. (2020b). The latter work combines the astrometric measurements from *Gaia* DR2 (Gaia Collaboration et al. 2018) with the available photometric and spectroscopic information to yield stellar radii with a median uncertainty of 4%. Starting from the DR25 planet catalog, we have removed planet candidates with: a) transit signal-to-noise ratio (S/N) below the nominal threshold (S/N= 7.1), b) NASA Exoplanet Archive [2] disposition flag being false positive, c) the derived planetary radius $R_{\rm p} > 20\,R_\oplus$, d) the orbital period $P > 400$ days, and e) the best-fit transit impact parameter $b > 1$. We restrict to Sun-like stars that are defined as main-sequence stars (as classified by Berger et al. 2018) with effective temperatures between 4700 K and 6500 K. The bulk of this section is about planets around Sun-like hosts, and

[1] A Gamma distribution can be parameterized in terms of a shape parameter α (> 0) and a rate parameter β (> 0). The probability density function of a variable x is $f(x;\ \alpha,\ \beta) = (\beta^\alpha x^{\alpha-1} e^{-\beta x})/\Gamma(\alpha) \propto x^{\alpha-1} e^{-\beta x}$, where $\Gamma(\alpha)$ is the Gamma function evaluated at α.

[2] exoplanetarchive.ipac.caltech.edu

topics such as correlations with various stellar properties, such as stellar mass, metallicity and binarity, are discussed in Section 2.5.

The baseline sample contains 2,525 planet detections around 98,213 Sun-like stars. Of all the transiting planets, 1451 are found in systems with only one detected transiting planet [3] and the remaining 1074 are from systems with multiple detected transiting planets. The average observed multiplicity rate, namely the average fraction of planets from known multi-planet systems, is 42.5%. This is a lower limit on the intrinsic multiplicity rate, as many of the single-planet systems seen in *Kepler* are likely part of intrinsic multi-planet systems (see details in Section 2.2). The observed transit multiplicity distribution in the sample is

$$(N_1,\ N_2,\ N_3,\ N_4,\ N_5,\ N_6,\ N_7) = (1451,\ 278,\ 97,\ 37,\ 12,\ 2,\ 1) \qquad 9.$$

and no system has more than seven transiting planets.[4] **Figure 2** illustrates the planets in our sample in the radius–period plane. Different multiplicities of transiting planets are shown with different symbols.

2.1. Planet distribution in the radius–period plane

With the above statistical sample we derive the planet frequencies in the Bayesian framework of Section 1.2. The parameter space in the radius–period plane is divided into logarithmically equally-spaced cells [5]. In each cell, the number of planet detections, $N_{\rm p}$, is found and the average detection efficiency, $\langle p \rangle$, is computed via

$$\langle p \rangle = \frac{\int_{R_{\rm p,min}}^{R_{\rm p,max}} \int_{P_{\rm min}}^{P_{\rm max}} (R_\odot/a) S(P,\ R_{\rm p}) d\ln P d\ln R_{\rm p}}{\int_{R_{\rm p,min}}^{R_{\rm p,max}} \int_{P_{\rm min}}^{P_{\rm max}} d\ln P d\ln R_{\rm p}}. \qquad 10.$$

Here $R_{\rm p,min}$, $R_{\rm p,max}$, $P_{\rm min}$, and $P_{\rm max}$ denote the boundaries of the cell, and $R_\odot/a$ is approximately the transit geometric probability at semi-major axis a around a Sun-like host. The sensitivity due to survey detection thresholds at a given period and radius, $S(P,\ R_{\rm p})$, is computed with the `KeplerPORTs` code, [6] which was first developed in Burke et al. (2015) and further updated for *Kepler* DR25 (Burke & Catanzarite 2017a) by incorporating results of transit injection and recovery tests for the final *Kepler* pipeline (Burke & Catanzarite 2017b, Christiansen et al. 2020). Updated stellar parameters were used to derive the mean sensitivity curve.

We adopt a flat prior on $\bar{n}_{\rm p}$, and its posterior distribution is then described by the Gamma distribution of **Equation 7** with $\alpha_0 = 1$ and $\beta_0 = 0$. For cells with ≤ 2 detections we report the 95% upper limits, whereas for the rest the means and the standard deviation given by **Equation 8** are reported as the measurements and associated uncertainties, respectively. We have verified that the deviation between the mean and the median is substantially smaller than the uncertainty for all relevant cells.

---

[3]We sometimes use the contraction "tranet" to stand for "transiting planet" in the text and figure legends and captions.

[4]Note that the only system in our sample with seven transiting planets, Kepler-90, has been found to contain one additional planet candidate (Shallue & Vanderburg 2018). However, this additional candidate was not found by the *Kepler* DR25 pipeline and thus not included.

[5]Since the typical precisions of planetary period and radius are much smaller than the cell sizes, we ignore the uncertainties of planetary parameters. See Foreman-Mackey et al. (2014) for how to incorporate the planet parameter errors in the analysis.

[6]The code is publicly available at `https://github.com/nasa/KeplerPORTs`.

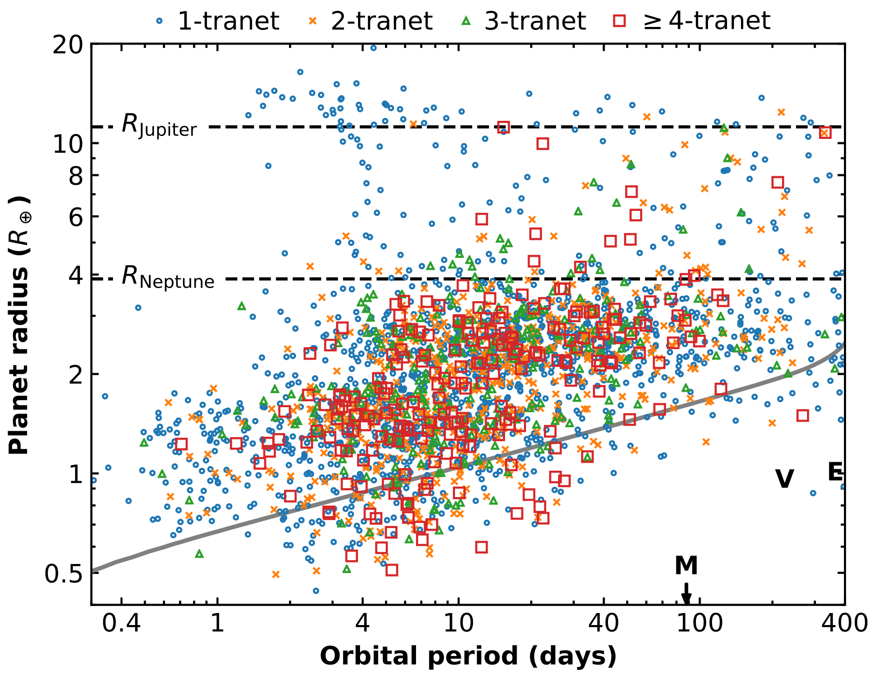


Figure 2

The close-in ($P < 400$ days) *Kepler* planets in the radius–period plane, with various symbols and colors indicating the observed multiplicity (note that we use the contraction "tranet" to refer to "transiting planet" in the legend). The gray solid curve indicates the median detection efficiency of the planet search pipeline. The solar system planets in the inner region, namely Mercury, Venus, and Earth, are denoted with their first letters. The median precision on the planetary radius is $\sim 7\%$. The radii of the Jupiter and Neptune are shown with horizontal dashed lines, respectively. The radius valley at $\sim 2\,R_\oplus$ (see Section 2.1.4) is visible.

The derived planet frequency map is shown in **Figure 3**. For cells with more than two detections, we also indicate the observed multiplicity rate of planets in the cell. Again, these multiplicity rates represent the lower limits on the fraction of planets in those cells that reside in multi-planet systems. We summarize several key results below:

- The integrated planet frequency is $\bar{n}_{\rm p} = 1.23 \pm 0.06$ for planets with radii in the range 1–20 $R_\oplus$ and orbital periods up to 400 days. This is broadly consistent with results from previous studies (e.g., Fressin et al. 2013, Petigura et al. 2018, Hsu et al. 2019). As stressed in Section 1.1, statistical analyses like this one do not yield the fraction of stars with planets $F_{\rm p}$, as the impact of the multiplicity and the mutual inclination has not been taken into account (see Section 2.2).
- As it has been clear since the earliest *Kepler* statistical studies, there are generally many more small planets with radii $R_{\rm p} \lesssim 4\,R_\oplus$ than larger ones, for orbital periods $P < 400$ days. Planet frequencies tend to increase from the upper left (large $R_{\rm p}$ and small P) toward the lower right (small $R_{\rm p}$ and large P). In other words, the

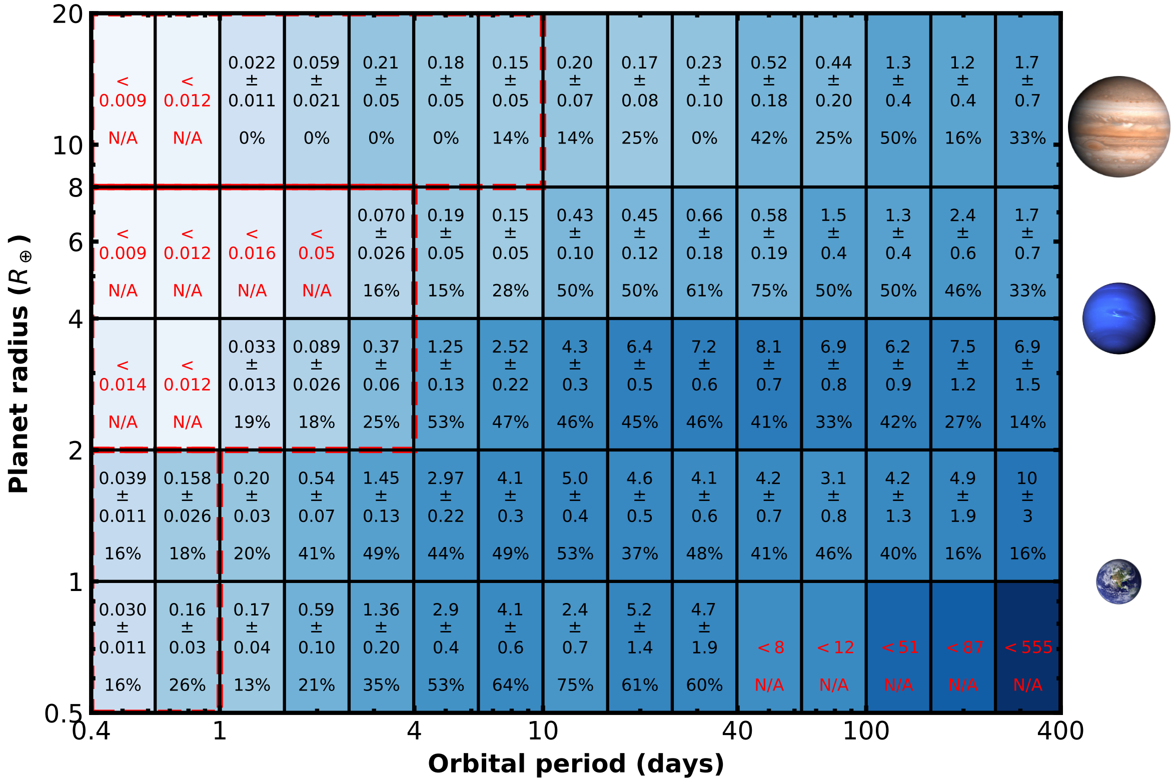


Figure 3

This figure illustrates the planet frequencies ($\bar{n}_\mathrm{p}$) and the observed multiplicity fractions based on the planet sample in **Figure 2**. The numbers and error bars are the average number of planets with periods and radii within the given cell per 100 Sun-like stars. If there are less than three detections found within the cell, then the 95% upper limit is reported instead. These upper limits are highlighted in red. The fraction in each cell denotes the observed multiplicity fraction, namely the fraction of planets in that cell found to reside in multi-planet systems. We use “N/A” for cells with less than three detections. The red dashed lines mark the regions corresponding to hot Jupiters, hot Neptune “desert,” and USPs.

intrinsic radius distribution is dependent on the orbital period (e.g., Dong & Zhu 2013, Foreman-Mackey et al. 2014, Hsu et al. 2018). There exist some local regions where the general trends break down, such as the radius valley (see Section 2.1.4).

- Sub-Earths ($R_\mathrm{p} < 1\,R_\oplus$) and Earth-sized planets in Earth-like orbits are not well probed by *Kepler*, and thus estimates of their frequencies are most susceptible to the uncertainties of survey sensitivity estimates. As a result, there remain large discrepancies on their intrinsic frequencies in the literature (see Table 2 of Winn & Fabrycky 2015 and Figure 17 of Burke et al. 2015).
- *Kepler* planets commonly reside in multi-planet systems in most parts of the radius–period plane, with some notable exceptions such as the hot Jupiter region (Steffen

et al. 2012; see Section 2.1.1 for more discussion). The intrinsic multiplicity rates are likely higher than the observed multiplicity rates shown in **Figure 3**. We defer to Section 2.2 for further discussions.

The above method to derive the planet frequency $\bar{n}_{\rm p}$ is non-parametric. An alternative approach employs a parameterized planet distribution function and then constrains the associated parameters. The parametric approach has been widely used in statistical studies of various detection techniques, including transit (e.g., Youdin 2011, Howard et al. 2012, Dong & Zhu 2013, Burke et al. 2015), RV (e.g., Tabachnik & Tremaine 2002, Cumming et al. 2008), and microlensing studies (e.g., Gould et al. 2010, Suzuki et al. 2016, Clanton & Gaudi 2016). It is also commonly used in simulations of generating synthetic planetary systems (e.g., Mulders et al. 2018, He et al. 2019). The commonly adopted planet distribution function is separable between the orbital period (or semi-major axis) and the planetary radius (or mass)

$$\frac{d^2N}{d\ln P d\ln R_{\rm p}} \propto \frac{dN}{d\ln P}\frac{dN}{d\ln R_{\rm p}}. \qquad 11.$$

The distributions of the orbital period and the planetary radius are usually parameterized as power laws or broken power laws. The use of such a separable function implicitly assumes that the period (radius) distribution is independent of the planetary radius (period). As discussed above, such an assumption is not valid for the inner planetary system. It is likely not valid for planet distributions in other regions of the parameter space, either. The implications of this failure on the derived occurrence rates from the parametric method and on the theoretical interpretations of the underlying population have not been fully explored.

In what follows, we provide brief discussions about selected regions in the radius–period plane.

2.1.1. Hot Jupiters. As the first type of exoplanets found around solar-type stars (Mayor & Queloz 1995), hot Jupiters ($8\,R_\oplus < R_{\rm p} < 20\,R_\oplus$ and $P < 10\,$days) remain interesting and exciting targets for both observational and theoretical purposes. Here we only review the occurrence and multiplicity rates of hot Jupiters in the current context and refer interested readers to the recent review by Dawson & Johnson (2018) for more in-depth discussions about the hot Jupiter population.

There is a long-standing discrepancy between the hot Jupiter frequency inferred from RV and transit surveys (e.g., Gould et al. 2006a, Wright et al. 2012; see Table B9 of Santerne et al. 2016 for an incomplete list). For example, our statistical sample yields a rate of $0.62 \pm 0.09\%$, which is in good agreement with previous studies of the hot Jupiter frequency in the *Kepler* field (e.g., Howard et al. 2012, Fressin et al. 2013, Santerne et al. 2016), whereas the RV surveys of stars in the Solar Neighborhood report rates that are typically a factor of $\sim$2 higher (0.9–1.2%; Mayor et al. 2011, Wright et al. 2012). It was suggested that the discrepancy could be caused by the different stellar properties, such as age, metallicity, and binary fraction, between the RV and transit samples. This has been tested by several follow-up studies of the *Kepler* sample. The *Kepler* stars are only slightly sub-solar on average ($\langle[{\rm Fe/H}]\rangle_{\rm Kepler} \approx -0.04$; Dong et al. 2014b), and their metallicity differences with the RV targets ($\langle[{\rm Fe/H}]\rangle_{\rm RV} \approx 0.0$) seem to be too small to fully account for the discrepancy even given the steep dependence of hot Jupiter frequency with metallicity (Guo et al. 2017). The unresolved binaries are also unlikely to substantially change the hot Jupiter frequency in the *Kepler* sample (Bouma et al. 2018). However, because RV surveys

preferentially exclude close ($\sim$ 1–50 AU) stellar binaries from their sample, this discrepancy in hot Jupiter frequencies between transit and RV surveys can potentially be resolved if the formation of hot Jupiters are suppressed in such close binary systems (Moe & Kratter 2019). Searching for stellar companions of transiting hot Jupiters (e.g., Ngo et al. 2016) and making comparisons with field stars is a promising way to further test this possibility.

As shown in **Figure 2**, one out of the 49 hot Jupiters in our statistical sample, Kepler-730b, has a nearby small planet companion (Zhu et al. 2018a, Cañas et al. 2019). As of writing, only two other hot Jupiters, WASP-47b (Becker et al. 2015) and TOI-1130c (Huang et al. 2020) are known to share the same property. Our statistical sample suggests that $\sim 2\%$ ($< 9.7\%$, 95% upper limit) of hot Jupiters have nearby ($\lesssim 20$ days), small ($\sim$1–4 $R_\oplus$) and nearly coplanar companions (see also Steffen et al. 2012 for the constraint on non-coplanar companions). This low multiplicity rate of hot Jupiters supports the general idea that most of them have undergone some large-scale migrations to arrive at current locations (e.g., Lin et al. 1996, Rasio & Ford 1996a, Weidenschilling & Marzari 1996). We refer to Dawson & Johnson (2018) for more in-depth discussions on this topic.

2.1.2. Hot Neptune "desert". The region $P \lesssim 4$ days and $2\,R_\oplus \lesssim R_{\rm p} \lesssim 8\,R_\oplus$ lands in the so-called hot Neptune (or sub-Jovian) "desert" (e.g., Szabó & Kiss 2011, Beaugé & Nesvorný 2013, Mazeh et al. 2016 and references therein), which is considered underpopulated, especially when inspecting mixed planet samples found in surveys with different detection sensitivities (e.g., ground-based transits and *Kepler*). This "desert" is however not that barren: the total planet frequency enclosed in the above region is $0.61 \pm 0.07\%$ from our statistical analysis (see **Figure 3**), making this hot Neptune "desert" similarly populated as the hot Jupiter region (see also Dong et al. 2018). While the above frequency is derived for a rectangular region in the radius–period plane, it is worth noting that the boundaries of this "desert" region are better described as a triangle and extend out to 5–10 d in $m_{\rm p}$ vs. a and $R_{\rm p}$ vs. P planes (see Figure 1 and Figure 4 of Mazeh et al. 2016). Dong et al. (2018) found that the frequency of planets inside this region depends on the host star metallicity in a way similar to the frequency of hot Jupiters, and they dubbed this population as "Hoptunes" (rather than "hot Neptunes") to reflect that not all of them were known Neptune-like physically. Out of our baseline sample of 61 planets in this region, 14 are observed to have planetary companions, and the periods for majority of these companions are within 10 d. The observed multiplicity rate is thus 23%, which is lower than the *Kepler* average while higher than that of hot Jupiters (see also Dong et al. 2018). We refer to Dawson & Johnson (2018) for more discussions on the connection of this population with close-in Jupiters and related theoretical implications.

A number of theories have been proposed to explain the formation of planets in this region (e.g., Kurokawa & Nakamoto 2014, Matsakos & Königl 2016, Lundkvist et al. 2016, Bailey & Batygin 2018, Owen & Lai 2018). The leading explanations of its triangular boundaries invoke photoevaporation (see more discussion in Section 2.1.4) and tidal effects following the high-eccentricity migration. The upper boundary is best explained as the tidal disruption barrier for gas giants following their high-eccentricity migrations (Matsakos & Königl 2016, Owen & Lai 2018). More massive planets can be tidally circularized closer to the star without tidal disruption, resulting in the negative slope of the upper boundary. It has been proposed that the same mechanism also produces the lower boundary, with the positive slope resulting from a mass–radius relation of small planets that is different from the relation of giant planets (Matsakos & Königl 2016). However, this mechanism may not

be able to explain the planets that are in or near the "desert" region and reside in multi-planet systems. An alternative theory, proposed by Owen & Lai (2018), suggests that the lower boundary is better explained by the photoevaporation of highly irradiated planets, and that the positive slope results from the fact that the photoevaporation mechanism is more effective if the planet is closer to the host star. There has been a growing interest of planets in this region with the TESS mission (e.g., Armstrong et al. 2020, Burt et al. 2020), and the follow-up studies of such planets will soon allow for a better understanding of their physical properties and formation mechanisms.

2.1.3. Ultra-short-period planets. Planets with radii between 0.5–2 $R_\oplus$ and periods $P \lesssim 1\,\mathrm{d}$, known as ultra-short-period planets (USPs), represent a rather extreme planet population. The period threshold for USPs at one day corresponds to an equilibrium temperature $\sim 2000\,\mathrm{K}$ for a Sun-like host, which is hot enough to sublimate dust grains. Below we briefly summarize several key properties of USPs and refer interested readers to the recent comprehensive review by Winn et al. (2018) for more discussions about this extreme planet population.

Our statistical analysis yields $\bar{n}_\mathrm{p} = (0.39 \pm 0.04)\%$ for USPs. This is in general agreement with the result of Sanchis-Ojeda et al. (2014), whose specialized pipeline yields $\bar{n}_\mathrm{p} = (0.51 \pm 0.07)\%$ for planets with radii in the range 0.8–2 $R_\oplus$ and $P < 1\,\mathrm{d}$. Out of the 81 USPs in our sample, 16 are found with outer planetary companions, indicating an observed multiplicity rate of 20%. The true multiplicity rate is probably much higher, since USPs can be largely misaligned relative to the outer planetary companions (Dai et al. 2018, Petrovich et al. 2019). In 13 of the 16 multi-planet systems involving USPs, the closest outer companion has $P_\mathrm{c} \lesssim 10\,\mathrm{d}$, and the USP is usually farther apart in terms of the period ratio from the rest of the planets in the same system (see also Steffen & Farr 2013).

The highly irradiative environment at sub-day orbit implies that USPs are unlikely to have formed *in situ*. Partially because of the comparable rates between hot Jupiters and USPs, it had been suggested that USPs could be the surviving cores of tidally disrupted hot Jupiters (Jackson et al. 2013), but this was not supported by several pieces of evidence including the lack of strong host metallicity dependence (Winn et al. 2017) and the relatively high multiplicity rate compared to hot Jupiters. A more plausible scenario is that the USPs have arrived at their current locations without losing much of their initial mass. One way of achieving this is the gradual decay of the orbit due to the tidal dissipation within the host star (Lee & Chiang 2017). Alternatively, the proto-USP planet may have been sent to an eccentric (and misaligned) orbit following the dynamical interactions with other planets in the system, and then the orbit decays and circularizes due to the tidal dissipation within the planet (Schlaufman et al. 2010, Petrovich et al. 2019, Pu & Lai 2019). This latter model sees its support in the relatively large mutual inclinations of USPs (Dai et al. 2018). Additionally, in order for the tidal inspiral model to produce USPs, the tidal dissipation in USP hosts needs to be efficient, but the population analysis on stellar kinematic ages seems to suggest otherwise (Hamer & Schlaufman 2020).

2.1.4. Radius valley. An important discovery in the field of exoplanet in recent years is the radius valley, which refers to a region in the radius–period plane at radii $R_\mathrm{p} \sim 2\,R_\oplus$ and periods between ∼3–30 days (Fulton et al. 2017, Van Eylen et al. 2018, Fulton & Petigura 2018). This radius valley is visible in our statistical sample (see **Figure 2**). The position of the valley in radius is reported to decrease with the orbital period (Van Eylen et al. 2018)

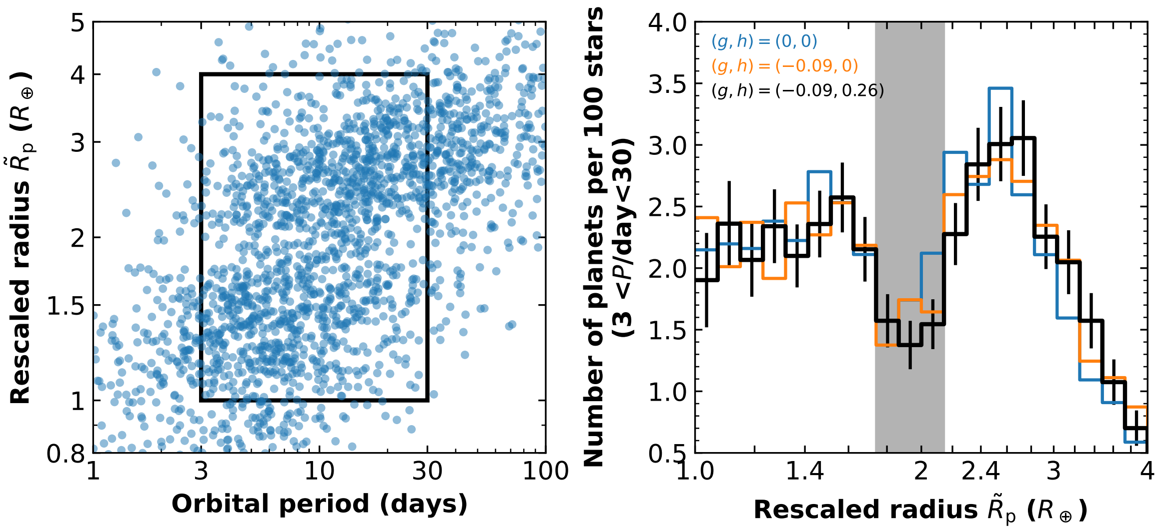


Figure 4

(*a*) The zoom-in view of the *Kepler* planets in our sample centered at the radius valley. The y-axis shows the rescaled radius $\tilde{R}_{\rm p} \equiv R_{\rm p}(P/10\,{\rm days})^{-g}(M_\star/M_\odot)^{-h}$ (see **Equation 12**) and we adopt the best-fit $g = -0.09$ (Van Eylen et al. 2018) and $h = 0.26$ (Berger et al. 2020a). The black box marks the boundary within which planets are used to derive the intrinsic radius distribution. (*b*) The intrinsic distribution of the rescaled radius $\tilde{R}_{\rm p}$. The radius gap, highlighted in the gray band, is most prominent when both period and stellar mass dependences are taken into account.

and increase with the stellar mass (Wu 2019, Berger et al. 2020a). The two dependences can be parameterized as

$$\frac{R_{\rm p}}{R_{\rm p}^{\rm valley}} = \left(\frac{P}{10\,{\rm days}}\right)^g \left(\frac{M_\star}{M_\odot}\right)^h . \qquad 12.$$

The valley position at orbital period $P = 10\,$days and host mass $M_\star = M_\odot$ is found to be $R_{\rm p}^{\rm valley} = 1.9 \pm 0.2\,R_\oplus$ and the slope quantifying the period dependence is $g = -0.09^{+0.02}_{-0.04}$ (Van Eylen et al. 2018). The slope quantifying the stellar mass dependence is $h = 0.26^{+0.21}_{-0.16}$ (Berger et al. 2020a). With the above relation one can then highlight the radius valley by rescaling the radius to $\tilde{R}_{\rm p} \equiv R_{\rm p}(P/10\,{\rm days})^{-g}(M_\star/M_\odot)^{-h}$. **Figure 4a** illustrates our sample in this rescaled radius (with $g = -0.09$ and $h = 0.26$) vs. orbital period plane. We also show the intrinsic distribution of the rescaled radius in **Figure 4b** for planets with $\tilde{R}_{\rm p}$ in the range 1–4 $R_\oplus$ and P in the range 3–30 days. Our choice of the period upper boundary is motivated by **Figure 2**: beyond $\sim 30\,$days the number of detections in the relevant region and thus the statistical power drops significantly. The peak-to-dip contrast in our "radius" distribution is not as significant as that shown in Fulton et al. (2017) and Fulton & Petigura (2018). In particular, our rescaled radius distribution does not show an obvious single peak at $\tilde{R}_{\rm p} < R_{\rm p}^{\rm valley}$. We have tried with the same period range as used in those studies and confirm that our specific choice of the period range is not the cause of this difference. One possible reason is the different statistical methods used to infer the occurrence rate: As discussed in Section 1.2, the IDEM approach used in Fulton et al. (2017) and Fulton & Petigura (2018) tends to underestimate the occurrence rates at

low sensitivity regions ($R_\mathrm{p} \sim R_\oplus$). The fact that the radius distribution does not seem to decrease at sub-Earth sizes suggests the presence of many undiscovered sub-Earths. The broader radius distribution may also imply that the planetary mass distribution is not as narrowly peaked as some previous studies inferred (e.g., Wu 2019).

The leading theory for the radius valley is the atmospheric evaporation driven by high-energy photons from the host star (photoevaporation; Owen & Wu 2013, Lopez & Fortney 2013, Owen & Wu 2017). In fact, the existence of the radius valley at approximately the discovered position had been predicted years before its discovery (Owen & Wu 2013, Lopez & Fortney 2013; see a historic overview in Owen 2019), which is exceptional in exoplanetary science. The photoevaporation of the atmosphere is thought to mostly take place during the early ages of the system when the star emits a higher fraction of its total luminosity at high energy ($\lesssim$ 100 Myr; e.g., Jackson et al. 2012, Tu et al. 2015, but also see King & Wheatley 2021). For close-in ($\sim$ 3–30 days) planets with core masses of a few $M_\oplus$, the high-energy radiation is sufficient to unbind the entire hydrogen/helium atmosphere if its initial mass fraction is below some critical value (a few percent; Owen & Wu 2017). The radius valley thus emerges, separating planets with and without extended atmospheres (Owen & Wu 2013, Lopez & Fortney 2013, Owen & Wu 2017). The observed period and stellar mass dependences can also be well explained by photoevaporation. As the orbital period increases and/or the host mass decreases, the amount of high-energy radiation the planet receives decreases and thus the valley moves to smaller radii (Owen & Wu 2017, Wu 2019).[7] We refer interested readers to Owen (2019) for a comprehensive review on the photoevaporation mechanism.

According to the photoevaporation theory, the properties (e.g., location and shape) of the radius valley depend on the underlying planetary properties, especially distributions of the core mass, core composition, and atmospheric mass fraction (Owen & Wu 2013, Lopez & Fortney 2013). Therefore, the observed radius valley opens up a venue to statistically infer the properties of close-in low-mass planets at birth (Owen & Wu 2017, Jin & Mordasini 2018, Wu 2019, Rogers & Owen 2020). Assuming that photoevaporation is the underlying mechanism, these studies collectively point to a typical core mass of a few $M_\oplus$, a core composition similar to that of the Earth (i.e., rich in silicate/iron and poor in water/ice), and a typical atmosphere mass fraction at birth of a few percent. These inferred properties have important implications to the formation and migration history of these close-in planets (see Section 4).

While photoevaporation has seen its success in predicting and explaining the radius valley, alternative theories exist that can also explain the observed valley (e.g., Ginzburg et al. 2018, Lee & Connors 2020), of which the core-powered mass-loss mechanism is considered the main competing theory. Unlike photoevaporation, the energy source for atmosphere stripping in core-powered mass-loss mechanism is the internal luminosity of the cooling core, and this process is expected to operate on much longer timescales ($\sim$ Gyr) (Ginzburg et al. 2018). The observed period and stellar mass dependences of the radius valley (**Equation 12**) are also consistent with this mechanism (Gupta & Schlichting 2019,

[7] Although later-type stars have higher fractions of the total luminosity emitted in higher energy ($\propto M_\star^{-3}$; Lopez & Rice 2018) and remain active for a longer period of time, these lower-mass stars have much lower total luminosities ($\propto M_\star^4$ for Solar and later-type stars). The lifetime-integrated high-energy radiation at a certain orbital separation is shown to decrease with decreasing stellar mass (see Figure 4 of McDonald et al. 2019).

2020). Similar to photoevaporation, core-powered mass-loss mechanism also supports that the close-in low-mass planets have predominantly rocky cores with low water-ice fractions (Gupta & Schlichting 2019).

Attempts have been made to identify which of the two mechanisms discussed above is more responsible for the observed features. These studies made use of either the different stellar mass or age dependences of the two mechanisms (e.g., Hirano et al. 2018, Berger et al. 2020a). However, the currently available data provide no conclusive result to distinguish between the two. Larger samples and/or more precise measurements of stellar properties will be needed.

2.2. Mutual inclinations and the intrinsic multiplicity

The mutual inclination distribution of planets in multi-planet systems conveys important information on the formation and dynamical evolution of planetary systems. However, currently employed detection techniques are usually incapable of directly measuring mutual inclinations. This is particularly true for RV and microlensing. The transit technique is strongly biased toward (nearly) coplanar systems. Nevertheless, advancements have made it possible to statistically infer the mutual inclination distribution from the *Kepler* data.

The key issue in constraining the mutual inclination distribution with transit is the strong degeneracy with the intrinsic multiplicity (e.g., Lissauer et al. 2011, Tremaine & Dong 2012). Specifically, with the observable multiplicity function of transit alone one cannot distinguish between high-multiplicity systems with large mutual inclinations and low-multiplicity systems with small mutual inclinations. We therefore combine mutual inclinations and intrinsic multiplicity in the same discussion.

Before discussing the statistically inferred mutual inclinations, we briefly overview a handful of systems with measured large mutual inclinations. By combining *HST* astrometry and ground-based RV measurements, McArthur et al. (2010) measured the mutual inclination between two of the three planetary companions in the Upsilon Andromeda system to be about 30°. Mills & Fabrycky (2017) performed photo-dynamical modeling of the transit timing variation (TTV) and transit duration variation (TDV) signals of the Kepler-108 system and found the mutual inclination to be $\Delta I = 24^{+11\,\circ}_{-8}$ between the two transiting planets. The pi Mensae system, which hosts a long-period giant planet and a TESS transiting super Earth (Huang et al. 2018, Gandolfi et al. 2018), is reported to have significant mutual inclinations ($\sim$ 30–150°) from joint analyses of the *Hipparcos* and *Gaia* DR2 astrometry (Xuan & Wyatt 2020, Damasso et al. 2020, De Rosa et al. 2020). Additionally, some USP systems have also been determined to have large mutual inclinations (e.g., Dai et al. 2018). More planetary systems with large mutual inclinations are expected to be found in the following years, especially with *Gaia*'s capability to determine the 3D orbital configurations (Perryman et al. 2014).

2.2.1. The weighted transit duration method.

A popular method to statistically infer the mutual inclination of *Kepler* muti-planet systems makes use of the ratio of transit chord lengths (Steffen et al. 2010)

$$\xi \equiv \frac{T_{\rm in} P_{\rm in}^{-1/3}}{T_{\rm out} P_{\rm out}^{-1/3}} = \sqrt{\frac{(1+r_{\rm in})^2 - b_{\rm in}^2}{(1+r_{\rm out})^2 - b_{\rm out}^2}}\ . \qquad 13.$$

The subscripts "in" and "out" denote values of the inner and the outer transiting planets, respectively. Here T measures the time from the first to the last contact points of transit, r is the planet-to-star radius ratio, and b is the transit impact parameter. As both T and period P are precisely measured from transit data (Seager & Mallén-Ornelas 2003), the parameter ξ is well determined from observations. The last expression in **Equation 13** is used to construct the ξ distribution from models with assumed mutual inclination distributions. When two transiting planets are exactly coplanar, the ratio $b_{\rm in}/b_{\rm out} = a_{\rm in}/a_{\rm out} = (P_{\rm in}/P_{\rm out})^{2/3}$ is precisely measured and thus the parameter ξ only concerns one poorly constrained fiducial parameter (either $b_{\rm in}$ or $b_{\rm out}$, since both $r_{\rm in}$ and $r_{\rm out}$ are reasonably well measured). The distribution of ξ for coplanar systems is thus expected to narrowly peak at unity. In practice, the observed distribution is not so narrow, because of the introduction of the mutual inclination (see **Figure 5a**).[8] Applying this weighted transit duration method to large samples of *Kepler* planet pairs, Fang & Margot (2012) and Fabrycky et al. (2014) found that the mutual inclinations between transiting planets in the *Kepler* multi-planet systems could be well described by a Rayleigh distribution with a dispersion of a few degrees ($\lesssim 3$–5°). This has been frequently interpreted as multi-planet systems being nearly coplanar. However, with the use of only transiting planet pairs, which preferentially have small mutual inclinations, the weighted transit duration method cannot well determine the higher end of the mutual inclination distribution. As an extreme case, even the isotropic distribution of orbital inclinations cannot be reliably ruled out with the use of transit data alone (Tremaine & Dong 2012).

2.2.2. "Kepler dichotomy". To recover the true mutual inclination distribution, one needs to break its strong degeneracy with intrinsic multiplicity. The first attempt was carried out by Lissauer et al. (2011). The authors tried different functional forms for the intrinsic multiplicity distribution (uniform, Poisson, and exponential) as well as for the mutual inclination distribution (uniform and Rayleigh; see also Sandford et al. 2019). By modeling the intrinsic multiplicity as a uniform (or Poisson) distribution and the mutual inclination as a Rayleigh distribution, Lissauer et al. (2011) were able to find matches to all observed transit multiplicities except the transit singles. Specifically, their models would under-predict the number of systems with only one transiting planets by nearly 50%. This signals the failure of their simplified model. Nevertheless, this feature was picked up by many others and phrased as the evidence for two distinct populations of planetary systems (the so-called "*Kepler* dichotomy"): In one population planetary systems have small mutual inclinations and relatively compact configurations, whereas in the other population planetary systems have either only one planet or at least two largely mutually inclined planets (e.g., Johansen et al. 2012, Ballard & Johnson 2016, Mulders et al. 2018, He et al. 2019). Taking the *Kepler* sample as a whole, in terms of distributions of many properties of stars (e.g., stellar mass, metallicity) and planets (e.g., period), transit singles and transit multis are statistically consistent with being drawn from the same parent population (e.g., Xie et al. 2016, Munoz Romero & Kempton 2018, Zhu et al. 2018b, Weiss et al. 2018a), suggesting that they probably have the same origin.

While modeling the mutual inclination as a Rayleigh distribution (or more generally, Fisher distribution; Tremaine & Dong 2012, Zhu et al. 2018b) seems a reasonable choice (see

[8]The orbital eccentricity e in principle also affects the ξ distribution, but its contribution is relatively minor and thus e cannot be well constrained with this method (Fabrycky et al. 2014).

also Tremaine 2015), the proper functional form for the intrinsic multiplicity distribution remains an open question. Nevertheless, it is certainly oversimplified to assume that all planetary systems have the same number of planets (e.g., Ballard & Johnson 2016, Mulders et al. 2018). Having a Poisson distribution for the intrinsic multiplicity (e.g., Lissauer et al. 2011, Zink et al. 2019, Sandford et al. 2019, He et al. 2019) is likely not justified, either. The underlying assumption behind the Poisson distribution is that occurrences and properties of individual planets around the same host are independent from each other. While it has not been proved invalid for *Kepler* planets, there is emerging evidence that the presence and properties of planets inside the same system may be correlated due to the shared formation environment and/or host properties (see Sections 1.1, 2.4 and 2.5). Furthermore, the exponential or power-law (i.e., Zipfian distribution; Sandford et al. 2019) forms can be securely ruled out. These distributions predict overly abundant intrinsic single-planet systems, which is not supported by TTV observations (see below).

Given the strong degeneracies, disentangling the intrinsic multiplicity function and the mutual inclination distribution therefore requires external information. To this end, Tremaine & Dong (2012) developed a general statistical framework to account for observational biases of different techniques. Applying their method to planetary systems found by *Kepler* and RV, Tremaine & Dong (2012) found that the mean mutual inclination dispersion, which was assumed to be the same for all multiplicities, should be $\lesssim 5^\circ$ and that the intrinsic multiplicity function could not be constrained. See Figueira et al. 2012 for a different attempt in combining *Kepler* and RV data.

Tremaine & Dong (2012) also pointed out an observational feature that was difficult for their models to explain. As originally noticed by Ford et al. (2011), the fraction of systems showing TTV signals does not seem to vary significantly with the transit multiplicity, except perhaps for very high (≥ 4) multiplicities (see also Xie et al. 2014). A similar feature also shows up in later large and uniform TTV searches, which consistently found that nearly half of the TTV detections were from systems with only one transiting planets (Holczer et al. 2016, Ofir et al. 2018). This indicates that planets in transit singles have almost the same probability to show TTV signals as planets in transit multis.

2.2.3. Multiplicity-dependent mutual inclinations. The assumption that the mutual inclination distribution is independent of the intrinsic multiplicity may not be valid. With all else being equal, the critical mutual inclination for long-term instability is probably dependent on the number of planets in the system (e.g., Pu & Wu 2015; see also Section 2.4.2). Observationally, one also finds that the distribution of the ξ parameter appears statistically different for different transit multiplicities. As shown in **Figure 5a**, lower transit multiplicities have broader ξ distributions that are suggesting larger mutual inclinations (see also He et al. 2020).

Zhu et al. (2018b) introduced the following relation between the mutual inclination dispersion, σ_i, and the intrinsic multiplicity (within *Kepler* window), k,

$$\sigma_i(k) = 0.8^\circ \left(\frac{k}{5}\right)^{\zeta} . \quad 14.$$

They applied the statistical framework of Tremaine & Dong (2012) and combined the transit and TTV statistics to infer the intrinsic multiplicity and mutual inclination distributions. TTV, as a detection technique (Agol et al. 2005, Holman & Murray 2005), applies to the same population of planetary systems as transit, and thus the combination of TTV and

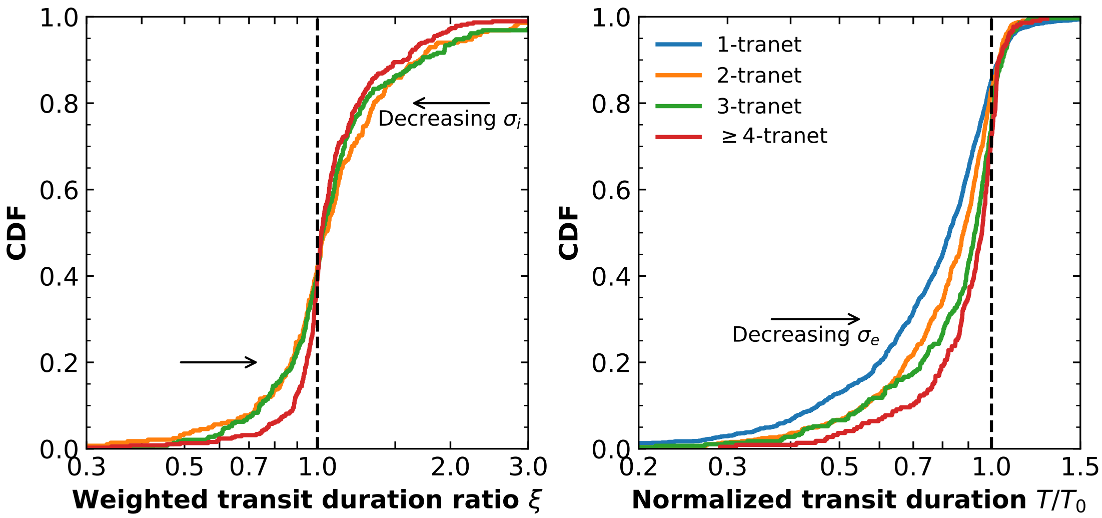


Figure 5

(a) The cumulative distribution functions (CDFs) of the weighted transit duration ratio, ξ (**Equation 13**), for different transit multiplicities. Larger transit multiplicities tend to have narrower ξ distributions, suggesting smaller mutual inclination dispersions σ_i. (b) The CDFs of the normalized transit duration, T/T_0 (**Equation 15**), for different transit multiplicities. Here T_0 is the transit duration for a circular and coplanar orbit. Larger transit multiplicities have narrower T/T_0 distributions, indicating smaller eccentricity dispersions σ_e.

transit is free from many assumptions and selection biases (compared to the use of RV; e.g., Tremaine & Dong 2012). Zhu et al. (2018b) found that the intrinsic multiplicity and the mutual inclination dispersion should be strongly correlated, with $-4 < \zeta < -2$ at the $2\,\sigma$ confidence level (see **Figure 6a** for an illustration). In other words, systems with fewer planets are dynamically hotter. This result also points to large mutual inclinations ($\gtrsim 10°$) for 2-planet and 3-planet systems. A recent work by He et al. (2020) found a qualitatively similar (although statistically different) result with a best-fit $\zeta = -1.7$ from modeling a collection of *Kepler* statistics (including transit multiplicities, the period distribution, period ratio distribution, etc) and imposing the angular momentum deficit (AMD) stability criterion (Laskar 1997, Laskar & Petit 2017) in simulated planetary systems. It is also worth noting that such a relation is steeper than the similar relation inferred from RV eccentricities (Limbach & Turner 2015), ergodic models (Tremaine 2015), or the extrapolations of the empirical stability boundary (e.g., Pu & Wu 2015).

Zhu et al. (2018b) also reported constraints on the intrinsic multiplicity vector, which is reproduced in **Figure 6b**. Although the individual components of the multiplicity vector are not well constrained, the summed fraction is well measured to be $30 \pm 3\%$ and does not rely on many assumptions like the other measurements do (see Section 5.1 of Zhu et al. 2018b; see also Section 1.1). The resulting average multiplicity in the *Kepler* parameter space is $\bar{m}_{\rm p} = 3.0 \pm 0.3$. This serves a lower bound on the average multiplicity in the inner ($\lesssim 1\,$AU) region, as smaller planets below the detection threshold of *Kepler* are unconstrained.

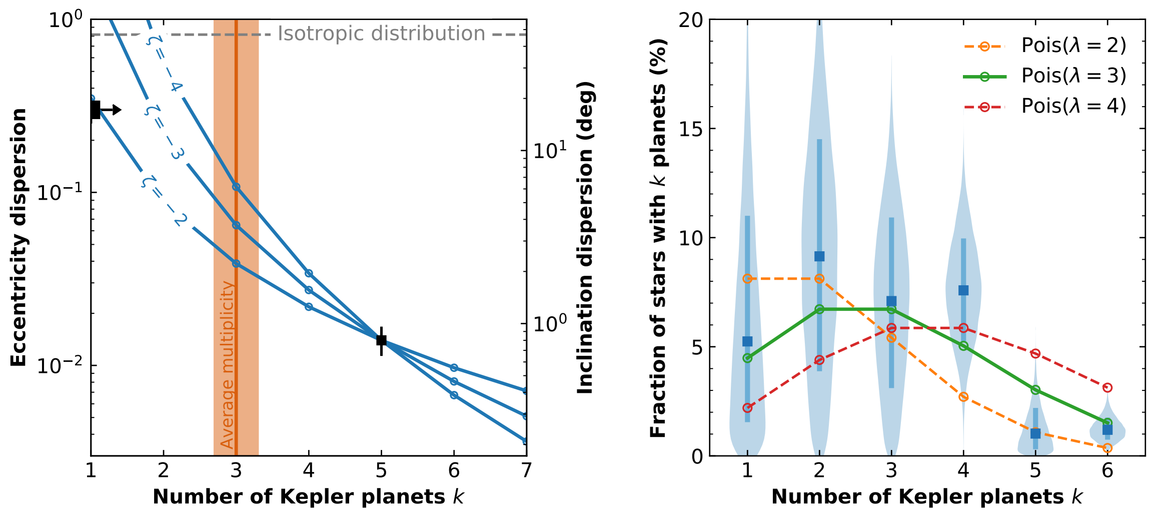


Figure 6

(*a*) Distributions of eccentricity and mutual inclination dispersions as functions of the intrinsic multiplicity. Here *Kepler* window is roughly the region above the gray curve in **Figure 2**. The relation $\sigma_e = \sigma_i$ is assumed (see Section 2.3.2). The ζ parameter quantifies the strength of the correlation with the intrinsic multiplicity (**Equation 14**). The orange band denotes the inferred average multiplicity $\bar{m}_{\rm p}$ for *Kepler* systems. The eccentricity dispersion inferred from transit singles (i.e., $k \geq 1$) and the mutual inclination dispersion constraint from systems with five *Kepler* transiting planets are shown as black squares. (*b*) The inferred intrinsic multiplicity vector and the associated probability distribution functions. The fraction of Sun-like stars with more than seven planets in the *Kepler* window is limited to $< 2.2\%$ (95% upper limit). The medians and the 16–84% ranges of individual components are denoted with squares and error bars, respectively. Poisson distributions with different values of mean parameter λ are shown for references. Both plots are adapted from Zhu et al. (2018b).

2.3. Eccentricity distribution

Similar to mutual inclinations, orbital eccentricities also provide important information on the formation and dynamical evolution of planetary systems. Here we focus on the eccentricity results from the *Kepler* sample. Readers can find discussions about eccentricities from RV in the Section 3.1 of Winn & Fabrycky (2015).

The majority of the eccentricity measurements of individual *Kepler* planets were made through modeling the TTV and TDV signals (e.g., Lithwick et al. 2012, Wu & Lithwick 2013, Hadden & Lithwick 2014, 2017). These studies have found that the eccentricities of *Kepler* planets in near-resonance pairs are typically small, with a Rayleigh dispersion of up to a few percent. However, the planets selected for such dynamical modelings are probably a biased sample, and thus the derived eccentricity distribution may not be representative of the more general population.

2.3.1. The transit duration method. The transit duration (between the first and the fourth contact points) is given by [9]

$$\frac{T}{T_0} = \sqrt{(1+r)^2 - b^2}\,\frac{\sqrt{1-e^2}}{1+e\sin\omega}\ . \qquad 15.$$

Parameters r, b, and T are the same as those in **Equation 13**, and ω is the argument of periapsis. The quantity T_0 measures the transit duration between the first (second) and the third (fourth) contact points of a planet with the same period but circular ($e = 0$) and edge-on ($b = 0$) orbit and is related to the mean density of the host star, $\rho_\star$, via

$$T_0 \equiv \frac{R_\star P}{\pi a} = 13\ \mathrm{hr}\left(\frac{P}{\mathrm{yr}}\right)^{1/3}\left(\frac{\rho_\star}{\rho_\odot}\right)^{-1/3}\ . \qquad 16.$$

With known parameters from transit modeling (b, r, P, and T) and the nuisance parameter ω assumed to follow a uniform distribution, the quantity T/T_0 can be used to constrain the statistical distribution of e, provided that the stellar mean density is precisely measured (Ford et al. 2008). With other parameters being the same, larger eccentricities lead to broader distributions of the T/T_0 ratio (see **Figure 5b**). The successful application of this method heavily depends on the accurate characterizations of the host stars. As a result, early attempts to study the *Kepler* sample were all limited by the systematic uncertainties in the stellar properties (e.g., Moorhead et al. 2011, Kane et al. 2012, Plavchan et al. 2014).

2.3.2. Multiplicity-dependent eccentricity distribution. Van Eylen & Albrecht (2015) applied a variant of the transit duration method to a carefully selected sample of *Kepler* multi-planet systems whose host stars were precisely characterized via asteroseismology. These authors found that the eccentricities of planets in their sample could be well described by a Rayleigh distribution with $\sigma_e \approx 0.05$. Using accurate spectroscopic stellar parameters from LAMOST, Xie et al. (2016) found similar nearly-circular orbits for planets in the *Kepler* multis, and they reported a much larger eccentricity dispersion ($\sigma_e \approx 0.3$) for *Kepler* planets in systems with single transiting planets. Both results have been confirmed by later works (Van Eylen et al. 2019, Mills et al. 2019).

The multiplicity-dependent eccentricity distribution goes beyond the single vs. multiple bifurcation. This is demonstrated in **Figure 5b**, where we show the cumulative distributions of the T/T_0 ratios derived from our planet sample for different transit multiplicities. Here we have used the stellar mean densities from isochrone fits by Berger et al. (2020b) and the values of T from the *Kepler* DR25 MCMC chains (Hoffman & Rowe 2017). As **Figure 5b** indicates, the distribution of T/T_0 ratio becomes narrower with increasing transit multiplicities. As the transit multiplicity can be viewed as a rough proxy of the intrinsic planet multiplicity, it is suggestive that planetary systems with more planets have smaller eccentricity dispersions. This is also qualitatively consistent with studies of the RV planets (Limbach & Turner 2015, Zinzi & Turrini 2017). Based on observations of solar system and the general expectation that the dispersions of orbital eccentricity and mutual inclination are proportional to each other (Ida et al. 1993, Tremaine & Dong 2012, Xie et al. 2016),

[9] Note that our definition of the transit duration follows that of Seager & Mallén-Ornelas (2003) and is different from that of Winn & Fabrycky (2015). The latter measures the duration between two points where the planetary center sits on the edge of the projected stellar surface (see Figure 2 of Winn 2010).

we may use the same relation between intrinsic multiplicity and mutual inclination dispersion (**Equation 14**) for the relation between intrinsic multiplicity and orbital eccentricity dispersion. The multiplicity-dependent eccentricity dispersion is also shown in **Figure 6a** (see also He et al. 2020).

The large eccentricities and mutual inclinations of *Kepler* low-multiples have important theoretical implications. The largest eccentricity that can be achieved via scatterings among small *Kepler* planets themselves can be roughly estimated as:

$$e_{\rm max} \sim \frac{v_{\rm esc}}{v_{\rm orb}} \approx \sqrt{\frac{2 m_{\rm p} a}{M_\star R_{\rm p}}} = 0.15 \left(\frac{m_{\rm p}/M_\star}{10^{-5}}\right)^{1/2} \left(\frac{a}{0.1\ {\rm AU}}\right)^{1/2} \left(\frac{R_{\rm p}}{2\ R_\oplus}\right)^{-1/2} . \qquad 17.$$

Here $v_{\rm esc}$ and $v_{\rm orb}$ are the surface escape velocity and orbital velocity of the planet, respectively. The evaluation takes the typical values of a *Kepler* planet. While the above scaling relation bears some significant uncertainties, the large eccentricities ($\sigma_e \approx 0.3$) and mutual inclinations ($\sigma_i \gtrsim 10^\circ$) observed in the low-multiplicity planetary systems are probably on the high end of the distribution. It suggests that these planetary systems may have undergone significant dynamical interactions among the inner planets themselves. Alternatively, other mechanisms may have been invoked to excite eccentricities and mutual inclinations to values larger than what the self-scatterings can achieve. One promising mechanism is the interaction between the inner system and the outer massive planets (e.g., Johansen et al. 2012, Huang et al. 2017, Pu & Lai 2020, and references therein). We return to this point in Section 3.2.

2.4. Intra-system variation

The intra-system variation, which is about the relative properties of planets around the same host, is useful in constraining the formation and evolution processes of planetary systems. It also concerns the statistical inference of exoplanets in general: In some statistical studies, planet detections from the same star are treated as independent events (see Sections 1.2 and 2.2); in some others, specific assumptions about the relative properties of planets in multi-planet systems must be made when synthetic systems are generated (e.g., Mulders et al. 2018, He et al. 2019). The derived statistics to some extent are subject to the validity of such assumptions.

2.4.1. "Peas in a pod?". Transiting planets in the same *Kepler* multi-planet systems preferentially have similar sizes. This feature has been noticed since the early days of the *Kepler* mission (Lissauer et al. 2011, Ciardi et al. 2013). Follow-up observations that provided improved characterizations of the host stars enabled further studies that tried to understand the nature of this feature (Weiss et al. 2018b, He et al. 2019, Zhu 2020, Weiss & Petigura 2020, Murchikova & Tremaine 2020). In particular, Weiss et al. (2018b) quantified the correlation between sizes of neighboring planets around the same host in their sample. To check the statistical significance of this correlation, they generated synthetic systems by randomly drawing planetary radii from the observed size distribution and then performed the same correlation test. The size correlations in their synthetic systems were much weaker than what they saw in real systems, and thus they concluded the pattern was astrophysical. Together with a similar result on the spacings between planets, Weiss et al. (2018b) concluded that planets in *Kepler* multi-planet systems have similar sizes and regular spacings, a pattern they termed "peas in a pod" (see also Millholland et al. 2017 for a similar claim

about *Kepler* planet masses). A later study by He et al. (2019) reached a similar conclusion. According to these authors, planetary systems that contain clusters of planets whose sizes and orbital periods are correlated produce a better match to the observed *Kepler* systems in terms of the joint statistics of transit depth distribution, period distribution, period ratio distribution, etc.[10]

Different opinions exist about the nature of the observed correlations. Zhu (2020) pointed out a detection bias that was underestimated in the statistical method of Weiss et al. (2018b). Because small planets can be detected around bright and quiet stars whereas large planets are only detectable around faint or noisy stars, the same transit detection threshold (i.e., a fixed S/N) naturally leads to varying planetary size thresholds in different systems. This, combined with the fact that smaller planets are more abundant, naturally leads to a size correlation in the observed transit pairs (see also Murchikova & Tremaine 2020). However, it appears that the apparent correlation in planetary sizes is too strong to be explained entirely by this detection bias alone (Zhu 2020).

Another factor that has not been fully explored is the contribution of the planets that are missing, due to large impact parameters or sub-threshold values of transit S/N, in known *Kepler* multi-planet systems. Our solar system is an excellent example to demonstrate this point. The four outer giant planets would be unlikely to be detected by a transit mission similar to *Kepler* because of their long orbital periods. Of the four terrestrial planets, Mercury and Mars are almost impossible to detect in transit due to their small sizes. Therefore, a *Kepler*-like mission would, if possible at all, most likely detect the Venus–Earth planet pair, which shows very similar sizes ($0.95\,R_\oplus$ vs. $1\,R_\oplus$) and masses ($0.82\,M_\oplus$ vs. $1\,M_\oplus$). However, this level of similarity is not representative among the solar system planet pairs.

The physical interpretation of the size correlation (if any) is also unclear. One interpretation is that planets "know" about their siblings, namely the formations of two neighboring planets are directly correlated (e.g., Kipping 2018, Mulders et al. 2018, Sandford et al. 2019, He et al. 2019, Gilbert & Fabrycky 2020). Another interpretation is that planets "know" about the system and the environment they formed in, namely the formations of planets in the same system are all related to some global properties (Murchikova & Tremaine 2020). In this latter case, the apparent correlation between planetary sizes is only a projection of the correlation between the individual planets and the host star (or the birth disk). This latter interpretation has some observational evidence. For example, the planet distribution is shown to depend on the orbital period (see Section 2.1) and stellar properties (see Section 2.5). Murchikova & Tremaine (2020) demonstrated with a toy model that the observed size correlation could be well reproduced if the planets "know" about the host star but do not "know" about their neighbor planets.

2.4.2. Orbital spacings. The relative positions of planets in *Kepler* multi-planet systems have also drawn lots of interest. The majority of the early studies focused on the period ratio distribution. As shown in **Figure 7**, *Kepler* systems contain very few planet pairs near/in low-order mean-motion resonances (see also Lissauer et al. 2011, Fabrycky et al. 2014). This is in contrast with earlier RV results that a substantial fraction of

[10]The clustered model of He et al. (2019) has more free parameters than their non-clustered model. However, the authors did not perform model comparisons to justify the introduction of more flexibilities. See Zhu (2020) for more discussions.

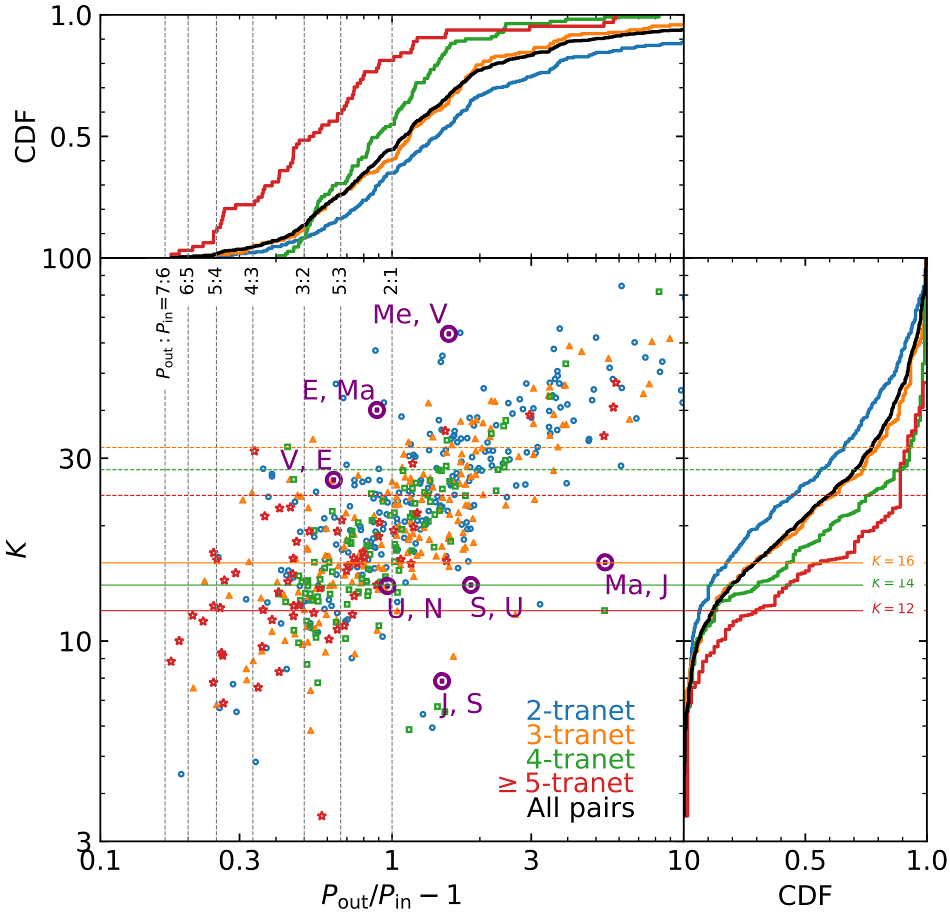


Figure 7

Spacings between the apparently adjacent planets in *Kepler* multi-planet systems, with different colors indicating planet pairs from different transit multiplicities. The x-axis of the main panel (lower left) shows the spacing in terms of the orbital period ratio, and the upper panel shows the corresponding cumulative distributions. A few example period commensurabilities are indicated in both panels. The y-axis of the main panel shows the spacing in terms of the mutual Hill radii (**Equation 18**), and the right panel shows the corresponding cumulative distributions. The stability thresholds for 3-tranet, 4-tranet, and 5-tranet systems, derived according to **Equation 20**, are indicated with solid horizontal lines. Values corresponding to twice of the thresholds are also shown as dashed horizontal lines. The code `Forecaster` from Chen & Kipping (2017) is used to predict the planet mass based on the planetary radius, and we have revised the upper mass limit to $10^3\,M_\oplus$ ($\sim 3\,M_{\rm J}$) to avoid masses beyond the planetary regime. Solar system planet pairs are also indicated for references.

well-characterized multi-planet systems contain pairs of giant planets close to mean-motion resonances (e.g., Wright et al. 2011). We refer to Section 4.1 for the theoretical implications of this feature. Additionally, the asymmetry around exact period commensurabilities has

also attracted lots of attention (Fabrycky et al. 2014), and we refer interested readers to the fairly comprehensive overview by Terquem & Papaloizou (2019) for this particular issue (see also the recent development by Millholland & Laughlin 2019). This review focuses on the dynamical compactness of the *Kepler* multi-planet systems, which concerns the long-term stability and thus the dynamical evolution.

When the stability of the planetary system is concerned, the orbital spacing between planets is usually expressed in the dimensionless parameter K

$$K \equiv \frac{a_{\rm out} - a_{\rm in}}{R_{\rm H}}; \quad R_{\rm H} \equiv \frac{a_{\rm in} + a_{\rm out}}{2} \left(\frac{m_{\rm in} + m_{\rm out}}{3M_\star}\right)^{1/3} . \qquad 18.$$

Here $R_{\rm H}$ is called the mutual Hill radius, $M_\star$ is the mass of the host star, and $a_{\rm in}$ ($a_{\rm out}$) and $m_{\rm in}$ ($m_{\rm out}$) are the semi-major axis and the mass of the inner (outer) planet, respectively. For two-planet systems, the condition for the long-term stability (and thus instability) has been well understood theoretically, and the instability arises when there are mean-motion resonance overlaps (Wisdom 1980, Deck et al. 2013, Hadden & Lithwick 2018). For systems with more than two planets, we lack a good theoretical understanding on the origin of the dynamical instability (see attempts by Chambers et al. 1996, Zhou et al. 2007, Quillen 2011, Yalinewich & Petrovich 2020). Nevertheless, numerical studies have shown that the timescale before which close encounter occurs between planets, t, scales exponentially with the initial spacing K (Chambers et al. 1996). Details of this scaling relation depend on factors such as the number of planets, planet masses, orbital eccentricities and inclinations, as well as the inhomogeneity among planets (e.g., Chambers et al. 1996, Zhou et al. 2007, Funk et al. 2010; see Pu & Wu 2015 for a recent summary).

In the context of *Kepler* planetary systems, Pu & Wu (2015) found through numerical simulations that the median spacing for stability could be approximated as

$$\langle K \rangle = 2.87 + 0.7 \log_{10} \tau + 2.4 \left[\left(\frac{\sigma_e}{e_{\rm H}}\right) + \left(\frac{\sigma_i}{4e_{\rm H}}\right)\right], \qquad 19.$$

where τ is the physical timescale t scaled by the orbital period of the innermost planet, $e_{\rm H}$ is the mutual Hill radius scaled by the semi-major axis of the innermost planet, and σ_e and σ_i are the dispersions of orbital eccentricities and mutual inclinations among the planets, respectively. With the multiplicity-dependent σ_e and σ_i (**Equation 14**) and the typical values for *Kepler* systems ($t \gtrsim$ Gyr old and the innermost planet of planet-to-star mass ratio $q \approx 10^{-5}$ at 0.1 AU), **Equation 19** yields

$$\langle K \rangle \approx 10.2 + 2.2 \left(\frac{k}{5}\right)^{\zeta} . \qquad 20.$$

With $\zeta = -2$ (Zhu et al. 2018b, He et al. 2020), planetary systems with (3, 4, 5) *Kepler* planets should have critical spacings $\langle K \rangle = (16,\ 14,\ 12)$, respectively.

We apply the above stability thresholds to the multi-planet systems from Section 2.1 and discuss the limitations. After the use of Kepler's third law, the only unknown to determine the spacing parameter K is the planet-to-star mass ratio. We estimate the planetary masses from the measured radii with the `Forecaster` code from Chen & Kipping (2017) and adopt the *Gaia* stellar mass from Berger et al. (2020b). Systems without reported stellar mass measurements are excluded. **Figure 7** illustrates the spacings between neighboring *Kepler* planets of all systems and systems divided into different transit multiplicities. For

transit multiplicities of 3, 4, and 5+, the majority ($\sim 70\%$) of planet pairs have spacings above the corresponding stability thresholds, confirming that they are indeed (most likely) long-term stable. The remaining $\sim 30\%$ planet pairs, considered long-term unstable by the above empirical thresholds, are probably stable as well. While part of this misclassification is due to the choice of fixed *Kepler* system parameters and the empirical (but sometimes unphysical) mass–radius relation (Chen & Kipping 2017), it nevertheless is a sign for the failure of the empirically determined stability criteria. In particular, these stability criteria do not take into account the impact of mean-motion resonances, which can be either protective or destructive to the involved planets.

Nevertheless, by applying the empirical stability thresholds to the data one finds that the majority of *Kepler* planet pairs are not far from the empirical stability limits: The median spacing of all planet pairs is $K \approx 20$, and about 80–90% of planet pairs from systems with at least three transiting planets have spacings within twice of the empirical stability thresholds (horizontal dashed lines in **Figure 7**). These results are consistent with previous findings (e.g., Fang & Margot 2013, Pu & Wu 2015, Weiss et al. 2018b) and also suggest that for the majority of *Kepler* planet pairs there is no room for inserting another (undetected) planet in between (Fang & Margot 2013). In other words, the observed *Kepler* planets are dynamically packed. However, it does not necessarily mean that *Kepler* systems do not contain additional planets. The space to the innermost and particularly the outermost *Kepler* planet allows the existence of additional planets without risking instability. For example, seven planets with $q = 10^{-5}$ are allowed per factor of 10 in semi-major axis if mutually separated by $K = 20$. The observed dynamically packed structure is also probably due to the selection bias that it is increasingly difficult for both planets in a wider-spacing pair to transit the host star.

As part of the "peas in a pod" claim (see Section 2.4.1), the spacings between *Kepler* planets in the same multi-planet system are found to be statistically similar (Weiss et al. 2018b). However, the observed correlation in spacings is driven by a small fraction ($\lesssim 5\%$) of systems containing the highest multiplicities, and the majority of systems do not show such a regular spacing pattern (Zhu 2020, Jiang et al. 2020).

2.5. Dependence of planet statistics on stellar properties

2.5.1. Impact of stellar companions. Stellar companions to the planet hosts affect the *Kepler* planet statistics in several ways. In transit surveys like *Kepler*, many of them appear unresolved and dilute the transit signals, potentially leading to misclassifications and erroneous planetary parameters (Ciardi et al. 2015, Bouma et al. 2018).[11] Thankfully, follow-up high-resolution imaging observations have been performed for nearly all *Kepler* planet candidates (e.g., Furlan et al. 2017, Ziegler et al. 2018, and references therein). For bright targets that contain Jupiter-like transits, Santerne et al. (2016) also performed systematic radial-velocity follow-up observations and identified a significant false positive rate (55%) for Jovian planet candidates. These efforts have led to a much better understanding of the impact of transit dilution on the *Kepler* planet statistics. In particular, Furlan et al. (2017) reported that about 10% (30%) of the candidate host stars have observed companions within $1''$ ($4''$), the majority of which are fairly faint compared to the target stars.

[11] Here an ambient star that is not physically associated with the target is also considered a companion to the target star.

In the most likely scenario that the transit signals come from the primary stars (see, e.g. Bouma et al. 2018), the dilution effect overall only affects the planetary radii up to a few percent on average (Furlan et al. 2017). This is within the uncertainty of *Gaia*-derived radii, and thus one does not expect it to have a significant impact on the general planet statistics. However, Earth-sized planets $R_p \lesssim 2\,R_\oplus$ are much more susceptible to the dilution effect, and thus the relevant statistics may suffer a more dramatic impact (Furlan et al. 2017, Bouma et al. 2018).

Besides the transit dilution effect, stellar companions can also affect the presence of planets through many dynamical processes (e.g., Artymowicz & Lubow 1994, Holman & Wiegert 1999). Very close ($a \lesssim 0.5$ AU) stellar binaries can host circumbinary (i.e., planetary-type or P-type) planets, and over a dozen such systems have been found (see Section 6.2 of Winn & Fabrycky 2015). We limit our discussions to the observational aspects of circumstellar (i.e., satellite-type or S-type) planets and the implications on planet statistics.

Studies based on RV and high-resolution imaging observations suggest that the existence of a close stellar-mass companion is usually associated with a lower frequency of circumstellar planets (e.g., Wang et al. 2014, 2015, Ngo et al. 2016, Kraus et al. 2016, Moe & Kratter 2019). The effect of binary on the presence of close-in planets is quantified by a suppression factor $S_{\rm bin}$, which is the ratio between the fraction of planet hosts with stellar companions and the fraction of field stars with the same type of companions (Kraus et al. 2016, Moe & Kratter 2019). Circumstellar planets are almost completely suppressed ($S_{\rm bin} \lesssim 15\%$) when the stellar companions are close (with separation $a_{\rm bin} \lesssim 10\,{\rm AU}$), regardless of the planetary size or observed multiplicities. Planets are nearly unaffected ($S_{\rm bin} \gtrsim 85\%$) if the stellar companions are distant ($a_{\rm bin} \gtrsim 100\,{\rm AU}$). At intermediate separations ($\sim$ 10–100 AU), the suppression effect gradually decreases with the increasing separation. See the Figure 3 of Moe & Kratter (2019) for a compilation of observational studies and an illustration of the suppression factor $S_{\rm bin}$ as a function of the binary separation.

With the above suppression effect and the known binary separation distribution, one can then infer the planet formation efficiency from the measured planetary system frequency $F_{\rm p}$. Moe & Kratter (2019) estimated that $F_{\rm bin} \approx 43\%$ of Sun-like primaries in a magnitude-limited survey like *Kepler* could not host close-in ($\lesssim 1$ AU) planets simply because of the influence of binary companions (see also Kraus et al. 2016). If these targets are excluded from the *Kepler* statistics, one finds that the formation efficiency of close-in planets around single stars, a parameter directly related to formation theories, should be $1/(1-F_{\rm bin}) = 1.8$ times higher than the fraction of stars with planets $F_{\rm p}$. This additional factor also provides a plausible explanation to the discrepancy in hot Jupiter frequencies measured from RV and *Kepler* (see Section 2.1.1).

2.5.2. Metallicity effect. Under the general assumption that the bulk metallicity of the host star is correlated to the total mass of building blocks available for planet formation, it is reasonable to believe that the planetary occurrence rate and properties may be correlated with the host star metallicity. For giant planets ($R_{\rm p} \gtrsim 8\,R_\oplus$ or $m_{\rm p} \gtrsim 0.3\,M_{\rm J}$) found by RV, it has been well established that their presence correlates strongly with the host metallicity (e.g., Santos et al. 2001, Fischer & Valenti 2005). This giant planet–metallicity correlation lends support to the core accretion model as the leading theory for the formation of giant planets (e.g., Pollack et al. 1996, Ida & Lin 2004b). Some recent studies have also claimed that hosts of eccentric giant planets are more metal-rich than hosts of nearly circular giant planets (Dawson & Murray-Clay 2013, Buchhave et al. 2018), but stronger statistical

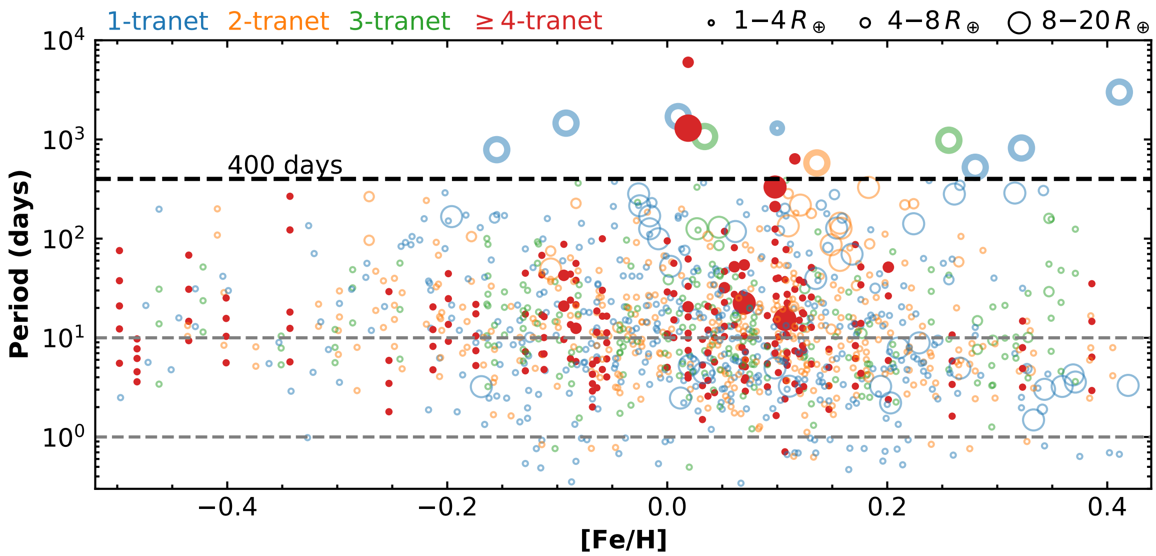


Figure 8

An illustration of the *Kepler* planetary systems in our baseline sample that have spectroscopic metallicity measurements. We use different colors to separate different observed multiplicities (out to 400 days) and different label sizes to separate planets of different sizes (small as 1–4 $R_\oplus$, intermediate as 4–8 $R_\oplus$, and giant as 8–20 $R_\oplus$). Cold ($P > 400$ days) planets found by RV (as tabulated in Zhu & Wu 2018) and long-period transit searches (Kawahara & Masuda 2019) are also indicated with thick circles. As the host metallicity increases, the system becomes more likely to contain giant planets at all periods and small planets at relatively close-in ($P \lesssim 10$ days) orbits (e.g., Mulders et al. 2016, Dong et al. 2018, Petigura et al. 2018). At very high metallicities ([Fe/H]$\gtrsim 0.2$), there seems to be a deficit of compact systems (with ≥ 4 transiting planets) and planets at intermediate orbits (∼10–400 days). These may be related to the emerging cold giants (Zhu & Wu 2018). The median metallicity of *Kepler* field stars is [Fe/H]≈ 0.0 (Dong et al. 2014b).

evidence is needed to fully establish this result.

Small planets, in particular those with radii $R_\mathrm{p} \lesssim 4\,R_\oplus$, show weaker dependences on host metallicity (e.g., Sousa et al. 2008, Buchhave et al. 2012). While many studies have focused on the dependence of the planet frequency $\bar{n}_\mathrm{p}$ on host metallicity (e.g., Wang & Fischer 2015, Petigura et al. 2018) and theoretical implications (e.g., Owen & Murray-Clay 2018, Lee 2019), one may argue that the planetary system frequency F_p is probably a more suitable parameter to characterize the efficiency of planet formation under such system-wide parameters like metallicity (Zhu et al. 2016, Zhu 2019). If the general planet–metallicity relation

$$F_\mathrm{p} \propto 10^{\gamma[\mathrm{Fe/H}]} \qquad 21.$$

is applied, the result of Zhu (2019) suggests $\gamma \approx 0.5$ for all *Kepler*-type planets, which is much weaker than the giant planet–metallicity correlation ($\gamma \approx 2$; Fischer & Valenti 2005). The dependence is further reduced if the close binaries that show anti-correlation with stellar metallicity are excluded from the statistics (Moe et al. 2019, Kutra & Wu 2020). Unlike the planetary system frequency F_p, the planet frequency $\bar{n}_\mathrm{p}$ does not appear to have a monotonic relation with the host metallicity. In particular, it may start declining when the metallicity is high enough (Zhu 2019). It has been suggested that this behavior may be

related to the formation of giant planets inside the same system: as the metallicity is high enough, the system has a significant probability to form giant planets, and these giants may reduce the multiplicity of the inner system either because they prohibit the formation of more small planets or because they dynamically remove some of the small planets out of the inner system. This scenario may also explain the increased diversity of planets around metal-rich *Kepler* hosts (Petigura et al. 2018) and the over-abundant compact planetary systems around metal-poor stars (Zhu & Wu 2018, Brewer et al. 2018). **Figure 8** displays along the host metallicity [Fe/H] the *Kepler* systems with metallicity measurements in our baseline sample.

While the stellar bulk metallicity measured in iron abundance [Fe/H] (or a mix of metals [m/H]) is usually used in studies of the planet metallicity dependence, other elemental abundances, in particular α elements and refractory elements, have also been looked for possible correlations with planet properties (e.g., Adibekyan et al. 2012, Liu et al. 2016, Teske et al. 2019). No clear trends have been found so far, probably due to the limited sample size, the measurement precision, and/or the impact of Galactic chemical evolution.

2.5.3. Dependence on stellar mass. A number of studies have also investigated the dependence of planet frequency on host mass. A theoretical possibility is that, the stellar mass correlates with the total mass in the protoplanetary disk and thus the amount of solid materials available for planet formation. It is largely consistent with direct observations of protoplanetary disks in (sub-)millimeter wavelengths (Andrews et al. 2013, Ansdell et al. 2016), although at a fixed stellar mass the scatters of inferred disk masses remain substantial (up to an order of magnitude; Ansdell et al. 2016).

We would like to start by pointing out several potential issues. Similar to the metallicity dependence (see Section 2.5.2), the two frequencies, $F_{\rm p}$ and $\bar{n}_{\rm p}$, can behave differently, especially for the small planets with high multiplicity rates. Second, as more massive stars also tend to be more metal-rich, one may need to carefully disentangle possible correlation between stellar mass and metallicity in the sample (e.g., Johnson et al. 2010, Kutra & Wu 2020). Furthermore, the choice of the parameter to study the correlation may matter. While planetary radius (or mass) and orbital period (or semi-major axis) are commonly used in statistical studies, Nature may prefer other physical units such as the planet-to-star mass ratio or the position of the water snow line (Hayashi 1981, Kennedy & Kenyon 2008; see **Figure 10** for an illustration). Last but not least, as far as the planet formation efficiency is concerned, one must correct for the suppression effect due to close stellar binaries (see Section 2.5.1). It is established that the close binary fraction correlates with the primary mass (e.g., Duchêne & Kraus 2013), so the suppression effect is expected to affect the statistics of planets around different stellar masses differently (Moe & Kratter 2019).

The dependence of giant planets on stellar mass has been investigated in many studies with different detection methods (e.g., Johnson et al. 2007, 2010, Howard et al. 2012, Fressin et al. 2013, Nielsen et al. 2019). To avoid many of the issues listed above, here we focus on the results from long-term RV surveys, as they cover a broad range of parameter space and are nearly free of close stellar binaries. In particular, Johnson et al. (2010) analyzed a sample of 1266 stars with at least 3-year RV observations and masses spanning from $0.2\,M_\odot$ up to their estimated $1.9\,M_\odot$, and reported a linear relation between the occurrence rate [12] and

[12] Their derived occurrence rate is technically $\bar{n}_{\rm p}$, but because of the low multiplicity rate of giant planets it closely approximates the rate $F_{\rm p}$.

stellar mass. This result has been widely considered as a benchmark in both theoretical and observational studies of giant planets. The higher-mass part of the sample come from the so-called "retired A-stars," and their spectroscopic mass estimates are controversial (Lloyd 2011, Schlaufman & Winn 2013, Malla et al. 2020 and references therein). Recently, the asteroseismic study by Malla et al. (2020) shows that the"retired A-stars" with spectroscopic masses $> 1.6\,M_\odot$ are overestimated, confirming the earlier reports by Lloyd (2011) and Schlaufman & Winn (2013). Since such stars consist of the heavier half of the Johnson et al. (2010) sample and contribute most of the statistical evidence to the reported stellar mass dependence (see the Figure 4 of Johnson et al. 2010), a revisit of the mass correlation will be needed. Additionally, the result of Johnson et al. (2010) is limited to the region with separation $a < 2.5\,\mathrm{AU}$. As shown by Clanton & Gaudi (2014) and Clanton & Gaudi (2016), after those at (slightly) larger separations are taken into account, giant planets are almost as common around M-dwarfs as they are around Sun-like stars (see Section 3.3).

For small planets, *Kepler* survey provides the best sample to study their stellar mass dependence. Studies have shown that the planet frequency $\bar{n}_\mathrm{p}$ in the *Kepler* parameter space is anti-correlated with stellar mass (e.g., Howard et al. 2012, Mulders et al. 2015a,b). Using the Berger et al. (2018, 2020b) sample with stellar effective temperature between 4000–5000 K, we find a frequency of $\bar{n}_\mathrm{p} = 3.3 \pm 0.4$ for planets in the radius range 1–20 $R_\oplus$ and period < 400 days, which is a factor of ~ 2.7 higher than the rate for our baseline Sun-like sample (Section 2.1). Later M-type stars have even more planets (Dressing & Charbonneau 2013, 2015). The planetary system frequency F_p is also anti-correlated with stellar mass but likely at a weaker level, due to the increased average planet multiplicity around later-type stars (e.g., Yang et al. 2020). There is some sign of increased observed multiplicity rate in our 4000–5000 K sample (48.2%) compared to that (42.5%) of our baseline Sun-like star sample (Section 2.1). After the correction for the suppression effect due to close stellar companions, the difference in formation efficiencies of small planets between single Sun-like and later-type hosts is likely further reduced, although an anti-correlation probably remains (Moe & Kratter 2019).

3. THE OUTER PLANET POPULATION

In the earliest stage of planet formation, the region beyond $\sim 1\,\mathrm{AU}$ is expected to contain most of the mass and the angular momentum of the protoplanetary disk. Therefore, the frequency and properties of planets in this outer region ($\sim$ 1–10 AU) have important implications to the formation and evolution of the whole system, including the planets in the inner $\sim 1\,\mathrm{AU}$ region. In this section, we review our current understanding of this outer planet population and discuss its connection with the inner planetary system.

We set the inner and outer boundary at $\sim 1\,\mathrm{AU}$ partly because this is approximately the detection limit of the *Kepler* mission, but also because it coincides with the position where giant planets show a rapid rise in frequency. RV surveys have found that giant planets ($m_\mathrm{p} \gtrsim M_\mathrm{Sat} \approx 0.3\,M_\mathrm{J}$) appear ~ 5 times more often between $\sim$ 1–3 AU than they do within $\sim 1\,\mathrm{AU}$ (Cumming et al. 2008).

3.1. Planet Frequency

RV surveys have found that cold giant planets (0.3–13 M_J) at $\sim$1–5 AU) appear around on the order of $\sim$ 10% of Sun-like stars. If the giant planet distribution is modeled as a

parametric function that joins single power-law distributions of mass and orbital period (Tabachnik & Tremaine 2002), the integrated rate out to $P \approx 5.5$ years is found to be $\bar{n}_{\rm p} = 0.105$ (Cumming et al. 2008). Such a single power-law period distribution tends to over-predict the number of giant planets at wider ($\gtrsim 10$ AU) separations. To better match the observed distribution, Fernandes et al. (2019) replaced it with a broken power law and found a potential peak at ∼2–3 AU (see also Bryan et al. 2016). Extending their distribution function out to 100 AU, Fernandes et al. (2019) found $\bar{n}_{\rm p} = 0.27^{+0.08}_{-0.05}$ and $0.062^{+0.015}_{-0.012}$ for planets in the mass range 0.1–20 $M_{\rm J}$ and 1–20 $M_{\rm J}$, respectively. If the frequency of the so-called Jupiter analogs, namely Jupiter-mass (∼0.3–3 $M_{\rm J}$) planets in Jupiter-like (a few AU) orbits around Sun-like hosts, are concerned, several independent studies have collectively pointed to a rate about a few percent (e.g., Wittenmyer et al. 2016 and references therein), suggesting that planetary systems similar to our own may be relatively uncommon (see also Section 3.2). Unlike our Jupiter, a significant fraction of cold giant exoplanets are on substantially eccentric orbits with typical eccentricities $e \sim 0.3$ (e.g., Wright et al. 2009). We refer to the review by Winn & Fabrycky (2015) for more discussions on these topics.

Although the region beyond ∼ 1 AU is nominally out of the reach of *Kepler*, studies have nevertheless systematically searched for and statistically studied the long-period transiting planets in the *Kepler* data (e.g., Foreman-Mackey et al. 2016, Herman et al. 2019, Kawahara & Masuda 2019). In particular, Herman et al. (2019) reported an occurrence rate of $\bar{n}_{\rm p} = 0.7^{+0.4}_{-0.2}$ for planets with sizes between 0.3–1 $R_{\rm J}$ and orbital periods between 2–10 years. The inferred radius distribution also suggests that cold Neptune-sized (3–5 $M_\oplus$) planets are ∼4 times more common than cold Jupiter-sized (7.5–11 $M_\oplus$) ones. This is broadly consistent with the result from microlensing surveys (see Section 3.3), pointing to the potential existence of a large and unexplored low-mass planet population in the outer region.

3.2. The inner–outer correlation

The planetary systems inside and outside of ∼ 1 AU appear strongly correlated. Such a strong inner–outer correlation has important implications to the formation and evolution of the system as a whole. Below we review the observational evidence and discuss briefly the implications of this correlation. More on the latter will be presented in Section 4.2. We highlight two classes of inner planets, hot Jupiters and super Earths, and discuss them separately below.

3.2.1. "Friends" with close-in Jupiters. Hot Jupiters, while usually having no detectable planetary companions in the inner region, are frequently found to have distant massive companions (Knutson et al. 2014, Bryan et al. 2016; but see also Schlaufman & Winn 2016). Both of these features are important clues to the formation and evolution of hot Jupiters, and we refer interested readers to the review by Dawson & Johnson (2018) for in-depth discussions.

For the completeness of the discussion about the inner–outer correlation, we briefly summarize here the key result of the "friends of hot Jupiters" search. Knutson et al. (2014) conducted a systematic RV study of the distant companions to a sample of 51 hot Jupiters and reported that each hot Jupiter should have on average 0.51 ± 0.10 companions with masses between 1–13 $M_{\rm J}$ and semi-major axes between 1–20 AU. This sample was reanalyzed in Bryan et al. (2016) with improved sensitivity calculations, and the companion rate was revised to 0.70 ± 0.08. Given the small fraction of systems with more than one cold

companion, we take this average number to be approximately the fraction of hot Jupiter hosts with cold Jupiter companions. This fraction barely changes after we adjust to the parameter range used in this work (0.3–13 M_J and 1–10 AU) according to the planet distribution function of Bryan et al. (2016). We denote this fraction as $P(\mathrm{CJ}|\mathrm{HJ})$. Additionally, given the known fractions of Sun-like stars with hot Jupiters and cold Jupiters, $P(\mathrm{HJ}) \approx 1\%$ and $P(\mathrm{CJ}) \approx 10\%$, respectively, the inversed conditional probability is $P(\mathrm{HJ}|\mathrm{CJ}) \approx 7\%$. This is the fraction of cold Jupiter hosts with hot Jupiters. All the four fractions are shown in **Figure 9**.

Jupiter-sized planets in the inner region with known outer giant companions tend to have higher eccentricities, suggesting possible dynamical interactions in sculpting the architectures of these systems (e.g., Bryan et al. 2016). In particular, warm ($\sim$ 10–100 days) Jupiters on significantly eccentric orbits ($e \gtrsim 0.4$) have much higher chances to possess relatively close ($\lesssim 3$ AU) Jovian companions compared to those on nearly circular ($e \lesssim 0.1$) orbits (Dong et al. 2014a), and the existence of such companions are consistent with the high-eccentricity migration scenario to form eccentric warm Jupiters (Dong et al. 2014a, Dawson & Chiang 2014, Petrovich & Tremaine 2016). By contrast, warm Jupiters on nearly circular orbits show a weaker correlation with outer giant companions, and many of these warm Jupiters are found to have nearby small planetary companions (Huang et al. 2016). These features cannot be easily reconciled in the high-eccentricity migration scenario, suggesting that the nearly circular warm Jupiters may have been formed *in situ* or have undergone the disk-driven migration (e.g., Raymond et al. 2008, Hallatt & Lee 2020). We refer to Dawson & Johnson (2018) for more comprehensive discussion on the observations and theories related to warm Jupiters.

3.2.2. Super Earth–cold Jupiter relation. The term "super Earth" has different meanings in different studies. Here we call a planet super Earth if its mass (or radius) is between the masses (or radii) of Earth and Neptune, and the correlation under discussion applies specifically to the super Earths from the inner region. These super Earths dominate the known inner planet population, and they can co-exist with almost all types of inner planets except hot Jupiters (see Section 2.1). For this reason, this super Earth population is representative of the inner planet population.

About 1/3 of the inner super Earths have outer cold Jupiter companions, as studies have shown (Zhu & Wu 2018, Bryan et al. 2019). The RV signal on the star induced by a super Earth is systematically smaller than the RV signal induced by a cold Jupiter. Making use of this point, Zhu & Wu (2018) constructed a sample of 54 super Earth systems around Sun-like hosts that received long-term RV observations, and they found that the fraction of super Earth hosts with cold Jupiter companions is $32 \pm 8\%$. This is ~ 3 times higher than the frequency of cold Jupiters around field Sun-like stars. The fraction further rises to $\sim 60\%$ for metal-rich systems (with [Fe/H]> 0.1). These results were later confirmed by the independent study of Bryan et al. (2019). In that work the authors refit RV data sets of 65 super Earth hosts, some of which are M dwarfs, and reported an occurrence rate of $39 \pm 7\%$ for companions with masses in the range 0.5–20 M_J and semi-major axes in the range 1–20 AU. In this review, we take a rather conservative value of $P(\mathrm{CJ}|\mathrm{SE}) \approx 30\%$, which is also shown in **Figure 9**.

The inversion of the above conditional probability reveals an even more interesting result. With $\sim 30\%$ of Sun-like stars hosting inner super Earths and $\sim 10\%$ of Sun-like stars hosting cold Jupiters, one finds from the Bayes theorem that $P(\mathrm{SE}|\mathrm{CJ}) \approx 90\%$,

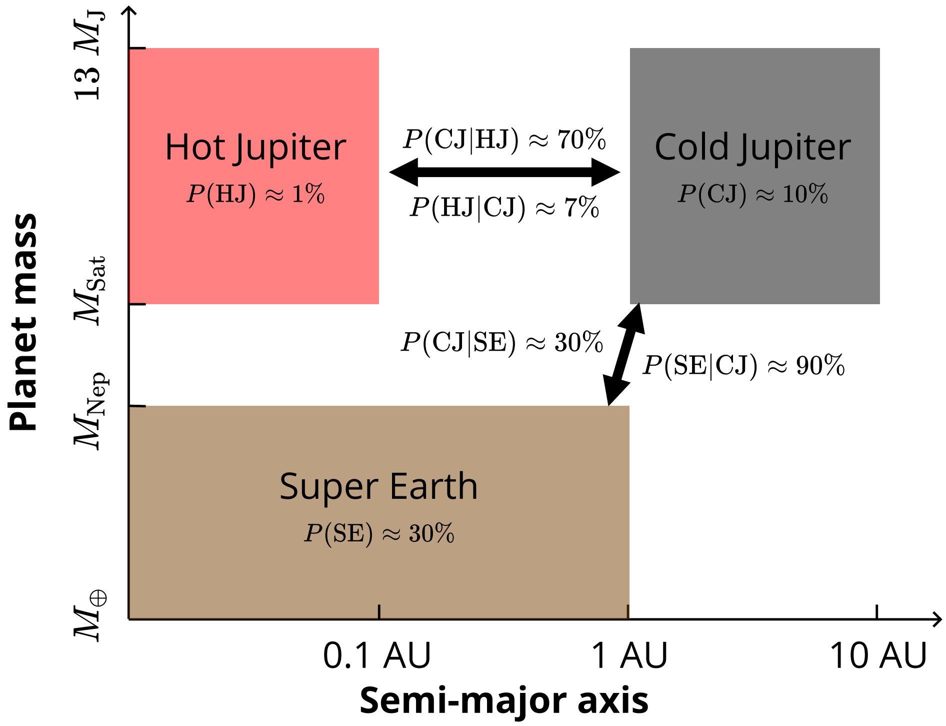


Figure 9

Correlations between inner planets and outer cold Jupiters. Although only two types of inner planets are highlighted here, they are representative of the known inner planet population: The majority of hot Jupiters do not have close neighbors (see Section 2.1.1), whereas super Earths usually reside in systems that include other types of inner planets (see Section 2.2). The unconditional probability shown here is the fraction of Sun-like stars with a specific type of planets, and the conditional probability is the fraction of Sun-like stars with a specific type of planets given that another type of planets is present in the system.

suggesting that nearly all of the cold Jupiters should have inner small planets (Zhu & Wu 2018, Bryan et al. 2019). Together with the fraction of cold Jupiter hosts with hot Jupiters, $P(\rm HJ|CJ) \approx 7\%$, outer giant planets almost all have inner companions.[13] We illustrate in **Figure 9** the connections between the outer giant planets and the two representative types of inner planets.

The above strong correlations are also confirmed by studies that utilized the rare but valuable long-period *Kepler* transiting planets (Uehara et al. 2016, Herman et al. 2019, Masuda et al. 2020). These studies find that the fraction of long-period ($P \gtrsim 2\,$years) transiting planets with inner transiting companions is so high that it can only be explained by a strong inner–outer correlation. They also reported evidence that the dynamical hotness of inner and outer planets may also be correlated. Specifically, a dynamically hot outer

[13]It is possible that hot Jupiters were born cold and that their later evolution had cleared out the small planets originally present in the inner region. This would mean that essentially all cold Jupiters were born with inner small planets.

Jupiter is likely associated with a dynamically hot inner planetary system. This provides a plausible explanation for the surprisingly large eccentricities and mutual inclinations of the inner systems with low multiplicities (Masuda et al. 2020; see Section 2.3). It may also help explain the reduced super Earth multiplicities around metal-rich stars (Zhu & Wu 2018; see Section 2.5.2).

The strong inner–outer correlation has implications on the frequency of planetary systems similar to our own. On the one hand, this correlation suggests that the general solar system-like architecture—with the inner region containing small planets and the outer region containing giant planets—is probably common among other planetary systems. On the other hand, planetary systems with properties very similar to ours, namely a system with both outer Jupiter-like ($\sim M_{\rm J}$ at a few AU) and inner Earth-like ($\lesssim M_\oplus$ within 1 AU) planets may be rare ($\lesssim 1\%$, Zhu & Wu 2018). A possible explanation could be that our Jupiter formed very early and hence prevented the growth of inner embryos into super Earths (Morbidelli et al. 2015, Izidoro et al. 2015). This early Jupiter formation scenario also explains the isotope measurements on solar system iron meteorites (Kruijer et al. 2017), although the question remains why the majority of cold Jupiters in other systems do have inner super Earths. We defer to Section 4.2 for further discussions of theoretical implications.

Observationally, the strong inner–outer correlation implies interesting synergies between space-based transit missions and astrometric missions or ground-based long-term RV surveys. Indeed, at least two of the TESS transiting planets have been found around stars with known RV cold Jupiters (Huang et al. 2018, Teske et al. 2020). Future combined TESS and *Gaia* planet catalogs should yield hundreds of similar systems that can enable detailed studies of the system architecture, as has been demonstrated in the pi Mensae system (Xuan & Wyatt 2020, Damasso et al. 2020, De Rosa et al. 2020).

3.3. Mass-ratio function from microlensing

Gravitational microlensing probes a largely uncharted planet discovery space of cold planets (Mao & Paczynski 1991, Gould & Loeb 1992), where $> 99\%$ of the planetary mass of the solar system resides. Ground-based microlensing surveys are sensitive to planets down to Earth masses (e.g., Bennett & Rhie 1996, Dong et al. 2006), and a space-based survey will be capable of discovering all solar system planet analogs except Mercury (Penny et al. 2019; see also **Figure 1**). With the increasing number of discoveries, microlensing searches have been continuing to unveil the distribution of planets in this under-explored parameter space and offer insights into the planet formation outside the water snow line. We refer interested readers to Gaudi (2012) for an overview of the microlensing technique and its application in exoplanet discoveries (see also Mao 2012). Below we focus on the important progress made since the review of Gaudi (2012).

Several recent studies found evidence for a possible turnover in the planet-to-star mass ratio function for planets beyond the water snow line (see **Figure 10**). In the early era, a key microlensing finding was that cold Neptunes (with planet-to-star mass ratio $q \sim 10^{-4}$) are a factor of a few more common than cold Jupiters (with $q \sim 10^{-3}$, Gould et al. 2006b), and Sumi et al. (2010) found that the distribution of the mass ratio q could be described by a power law $dN/d\log_{10} q \propto q^{\nu}$, where $\nu = -0.7 \pm 0.2$. Using the planet sample from the MOA-II microlensing survey, Suzuki et al. (2016) found that a single power law of the mass ratio function does not extend to very low mass ratios. Specifically, these authors reported a break in the mass ratio function at $q \sim 10^{-4}$, corresponding to the mass of

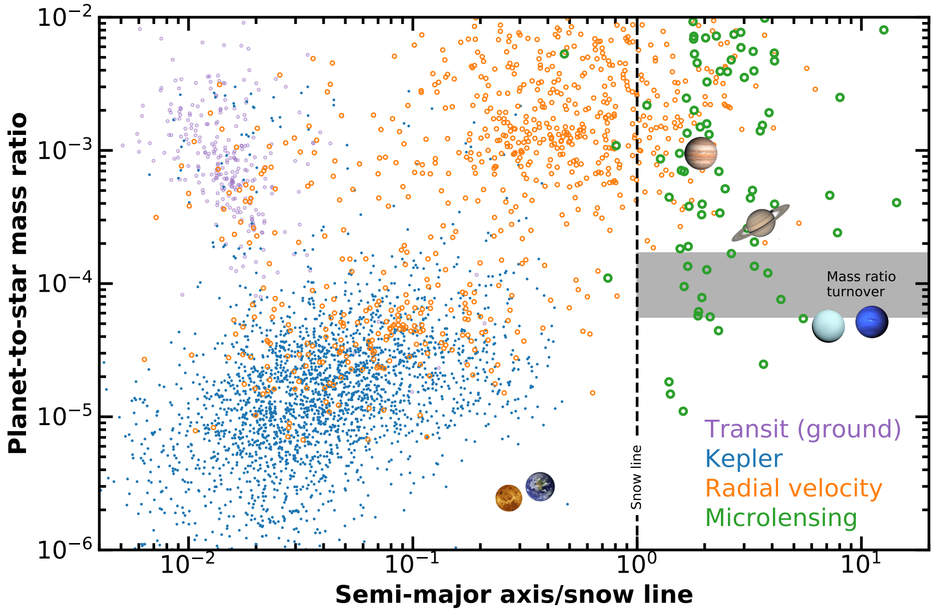


Figure 10

Similar to **Figure 1**, but here shows the planet-to-star mass ratio vs. the semi-major axis in units of the water snow line. The snow line is at 2.7 AU for 1 $M_\odot$ star and scales linearly with the host mass (Kennedy & Kenyon 2008). The location of the snow line is indicated with a black dashed line (note that this is only for illustrative purposes as the snow line should be determined in the protoplanetary disk), and the possible turnover in the mass ratio distribution found from microlensing, 0.55–1.7 $\times 10^{-4}$ (Suzuki et al. 2016, Jung et al. 2019), is marked with the gray region. Six solar system planets are shown, with Mercury and Mars too low in mass ratio to appear on this plot.

Neptune for a typical host star mass of 0.5 $M_\odot$. Based on a total sample of 30 planets that combines the MOA-II and previous statistical samples (Gould et al. 2010, Cassan et al. 2012), Suzuki et al. (2016) reported a broken power-law mass ratio function with a break at $q_{\rm brk} = 1.7 \times 10^{-4}$. The power-law indexes above and below the break are $\nu = -0.93 \pm 0.13$ and $0.6^{+0.5}_{-0.4}$, respectively. The normalization is such that $\bar{n}_{\rm p} = 0.79$ for planets with mass ratio $q > 5 \times 10^{-5}$ and projected separation s in units of Einstein radius in the range 0.3–5. For typical microlenses with 0.5 $M_\odot$, these numbers correspond to the planetary mass $M_{\rm p} > 8\,M_\oplus$ and the orbital separation between 1–15 AU. The reported planet frequency is compatible with those from other detection techniques (i.e., RV and direct imaging) following a simple joint planet distribution function (Clanton & Gaudi 2014, 2016).

Further studies by Udalski et al. (2018), who studied an ensemble of seven (as compared to four in Suzuki et al. 2016) planets with $q < 10^{-4}$, and Jung et al. (2019), who analyzed a sample of 15 planets with $q < 3 \times 10^{-4}$, investigated the possible turnover in the mass ratio function. Adopting a power-law form of the detection efficiency, Jung et al. (2019) modeled the intrinsic mass-ratio distribution with a broken power law and revised the break to $q_{\rm brk} \approx 5.5 \times 10^{-5}$, which is a factor of three below the value found by Suzuki et al.

(2016), but their low-mass planet sample was too small to distinguish a pile-up at that mass ratio from broken power law. Nevertheless, a break or pile-up in the planet-to-star mass ratio function could have important theoretical implications (e.g., Pascucci et al. 2018, Wu 2019), and further probing the distribution of sub-Neptune microlensing planets will be a research focus in the near future. Observations from high-cadence and nearly continuous microlensing surveys such as KMTNet (Kim et al. 2016) are pushing toward detecting more planets at low mass ratios (e.g., $q = 1.8 \times 10^{-5}$ from Gould et al. 2020a, $q \approx 1.4 \times 10^{-5}$ from Yee et al. 2021, $q \approx 1.1 \times 10^{-5}$ from Zang et al. 2021), so a large enough sample is expected to be available soon to improve the determination of the mass ratio function at the low end (see Zang et al. 2021 and discussions therein).

Another interesting feature of the mass ratio function of Suzuki et al. (2016) is its apparent smoothness between Neptune and Jupiter masses. Intriguingly, the derived radius distribution of cold planets from the single transit events in *Kepler* also appears similarly continuous between Neptune and Saturn (Herman et al. 2019). These results are surprising in view of the standard core accretion theory (Pollack et al. 1996), which builds on the solar system and predicts a deficit of planets at such intermediate masses/radii (Ida & Lin 2004a, Mordasini et al. 2009). This tension may suggest that the giant planet formation involves physical processes that have been overlooked in the standard models (Suzuki et al. 2018). Alternatively, it could be due to the limited sample sizes of cold intermediate-mass planets (Suzuki et al. 2016 sample contains nine detections in the range $10^{-4} < q < 5 \times 10^{-4}$ and Herman et al. 2019 has four in their intermediate radius bin of 0.67–1.00 $R_{\rm J}$). Therefore, increasing the sample size of cold intermediate-mass planets will clarify the degree of tension between observation and theory. Furthermore, physical mass (rather than mass ratio) determinations of a large sample of microlensing planets through measurements of the microlensing parallax or the lens flux (e.g., Dong et al. 2009) are needed to enable a more direct comparison with theories. This will be possible for essentially all microlensing planets detected to date at first light of adaptive optics on 30m class telescopes (e.g., Skidmore et al. 2015) or for a significant fraction of planet hosts in a space-based microlensing survey such as the *Roman* microlensing survey (Penny et al. 2019).

3.4. Free-floating planets

The prevalence of eccentric and/or inclined planetary orbits suggest likely histories of violent dynamical interactions in the planetary systems, such as planet-planet scatterings, which naturally eject a significant fraction of the planets from the system and form unbound planets with no hosts (e.g., Rasio & Ford 1996b, Jurić & Tremaine 2008, Chatterjee et al. 2008). The distributions of free-floating planets bear important signatures of not only the initial configurations of the planetary systems at birth, but also their subsequent dynamical evolution.

While it is possible to directly image young sub-stellar objects down to a few Jupiter masses (see, e.g., Zapatero Osorio et al. 2000), gravitational microlensing is the only known method in probing the lower-mass objects, which are believed to dominate the dynamically ejected FFP population. Low-mass objects produce relatively short-timescale microlensing light curves as the Einstein radius crossing time $t_{\rm E} \propto \sqrt{M}$. For typical stellar-mass microlenses, the timescale is ~ 20 days, whereas for planetary-mass objects it is $\lesssim 1$ day. The detection of such short and rare events thus demands wide-field high-cadence surveys that have only been available since the past decade.

Mróz et al. (2017) analysed a sample of 2,617 microlensing events from the OGLE-IV survey and concluded that the frequency of Jupiter-mass free-floating (or wide-orbit) planets should be no more than 0.25 planets per main-sequence star at the 95% confidence level. This result is broadly compatible with the inferred occurrence rate of bound giant planets from RV surveys (e.g., Cumming et al. 2008), microlensing searches (e.g., Gould et al. 2010) or direct imaging (e.g., Bowler 2016), and contradicts a previous claim that free-floating Jupiter-mass planets are more abundant than stars (Sumi et al. 2011). The sample of Mróz et al. (2017) also includes six short events with timescales in the range $0.1\,\text{days} < t_{\rm E} < 0.4\,\text{days}$. Assuming the microlensing nature of these events and given the low detection efficiency at such ultrashort timescales, their sample suggests that there may be up to a few free-floating planets in the Earth-mass to super-Earth-mass range per main-sequence star. The results of Mróz et al. (2017) about the absence of free-floating Jupiter-mass planets and the potential existence of free-floating Earth-mass and super-Earth-mass planets are generally consistent with theoretical expectations (e.g., Ida et al. 2013, Ma et al. 2016).

The existence of such ultrashort-timescale events was soon confirmed thanks to the coordinated observations of multiple microlensing survey telescopes around the globe. Mróz et al. (2018) reported the first convincing example of a microlensing event with timescale $t_{\rm E} = 0.32\,\text{days}$, and subsequent dedicated searches led to the discovery of a few more similar events (Mróz et al. 2019, 2020b,a, Kim et al. 2020, Ryu et al. 2020). These events all show strong finite-source effects that arise from the lenses *transiting* distant giant sources, yielding the immediate measurement of the angular Einstein radius $\theta_{\rm E}$. The lens mass scales as

$$M(\text{bulge}) = \frac{\theta_{\rm E}^2}{\kappa \pi_{\rm rel}} = 250\, M_\oplus \left(\frac{\theta_{\rm E}}{10\,\mu\text{as}}\right)^2 \left(\frac{\pi_{\rm rel}}{16\,\mu\text{as}}\right)^{-1}, \qquad 22.$$

with the normalization of the lens-source relative parallax $\pi_{\rm rel}$ chosen such that the lens and source are both in the Galactic bulge and separated by about 1 kpc. Here the constant $\kappa \approx 8.14\,\text{mas}\,M_\odot^{-1}$. For lens in the Galactic disk ($\pi_{\rm rel} \approx 125\,\mu\text{as}$), the mass scales as

$$M(\text{disk}) = \frac{\theta_{\rm E}^2}{\kappa \pi_{\rm rel}} = 32\, M_\oplus \left(\frac{\theta_{\rm E}}{10\,\mu\text{as}}\right)^2 \left(\frac{\pi_{\rm rel}}{125\,\mu\text{as}}\right)^{-1}. \qquad 23.$$

Kim et al. (2020) and Ryu et al. (2020) argue that $\theta_{\rm E}$ is a better discriminator than $t_{\rm E}$ for selecting FFPs. In fact, from a small number of events with finite-source effects, there is a possible gap between $\sim 10\,\mu$as and $\sim 30\,\mu$as in the $\theta_{\rm E}$ distribution, and this "Einstein desert" may separate brown dwarfs from free-floating super Earths (and terrestrial planets) in the disk (Ryu et al. 2020). We list in **Table 1** the relevant parameters and inferred masses of the FFP candidate events with $\theta_{\rm E} < 10\,\mu$as. The preliminary analyses by Mróz et al. (2019) and Ryu et al. (2020) suggest that low-mass unbound (or wide-orbit) planets may be more common than stars in the Galaxy. Future space-based microlensing surveys can assemble a large sample for quantitative assessments of the FFP population (e.g., Johnson et al. 2020), and a satellite augmented with microlensing parallax measurements can directly measure the masses and distances of such FFP events (e.g., Gould et al. 2020b, and references therein).

While the events listed in **Table 1** are promising candidates for FFPs, it is also plausible that these objects are actually in such wide orbits that no microlensing signatures from their hosts were detected. Light curve analyses can exclude the existence of any massive companions (i.e., hosts) out to a few Einstein radii, corresponding to $\sim$ 15–20 AU away

Table 1 Published microlensing free-floating planet candidates ($\theta_E < 10\mu$as), sorted by the inferred lens mass (see Equation 22 and Equation 23 for typical estimates in the bulge and disk, respectively).

Event name	θ_E/μas	t_E/d	M(disk)	M(bulge)	Reference
OGLE-2016-BLG-1928	0.84	0.029	$0.2\,M_\oplus$	$1.8\,M_\oplus$	Mróz et al. (2020a)
OGLE-2012-BLG-1323	2.4	0.16	$1.8\,M_\oplus$	$14\,M_\oplus$	Mróz et al. (2019)
OGLE-2019-BLG-0551	4.4	0.38	$6.1\,M_\oplus$	$48\,M_\oplus$	Mróz et al. (2020b)
KMT-2019-BLG-2073	4.8	0.27	$7.6\,M_\oplus$	$59\,M_\oplus$	Kim et al. (2020)
KMT-2017-BLG-2820	5.9	0.29	$11\,M_\oplus$	$87\,M_\oplus$	Ryu et al. (2020)
OGLE-2016-BLG-1540	9.2	0.32	$28\,M_\oplus$	$217\,M_\oplus$	Mróz et al. (2018)

(e.g., Mróz et al. 2018, Kim et al. 2020). In other words, these FFP candidates could well be planets at Uranus-like or Neptune-like orbits (e.g., Poleski et al. 2014). Future high-resolution imaging observations that can resolve the hosts for wide-separation planets will be able to tell whether these objects are truly free-floating or loosely bound to some unidentified stellar hosts (Han et al. 2005, Gould 2016, Ryu et al. 2020).

4. THEORETICAL IMPLICATIONS

The observed distribution of planets and the architecture of planetary systems, as reviewed in Sections 2 and 3, are the consequence of ∼10–100 Myr formation and later ∼Gyr evolution. In this section, we discuss the constraints from these observations on theoretical models. A comprehensive overview on the formation and evolution theories is beyond the scope of the current review. Instead, we focus on the key physical processes that lead to observational signatures. To reduce the complexity, we restrict to planetary systems around Sun-like hosts.

4.1. A brief overview of theories

The generally accepted picture of planet formation can be traced back to the nebular model originally proposed by Immanuel Kant and Pierre Laplace in the 1700s. Modern theorists generally believe that planets were formed out of the gas and the dust in the protoplanetary disk. Small solid particles first accumulate to form asteroid-sized (∼1–100 km) planetesimals, and the collisions between planetesimals eventually lead to the formation of planet-sized objects (Chamberlin 1916, Safronov 1972). See Woolfson (1993) for a historical overview on the planet formation theories.

In the core accretion theory that explains the solar system formation(e.g., Lissauer 1993, Pollack et al. 1996), the primary building blocks for planet formation are planetesimals. The growth of planetesimals is first divergent (i.e., the run-away phase) and then convergent (i.e., the oligarchic phase), until they have cleared nearly all planetesimals in their feeding zone ($\sim 5\,R_H$). These so-called protoplanets (or embryos) are now $\gtrsim 1000$ km in size and around Mars-mass (e.g., Ida & Makino 1993, Kokubo & Ida 1998). The further growth of the protoplanets involves planetesimal accretion as well as dynamical interactions between protoplanets. At a few AU separation, the growth of protoplanets is sufficient and allows the formation of giant planets (Mizuno 1980, Pollack et al. 1996). In the classical picture, the giant planet formation has three phases: core formation, hydrostatic gas accretion, and run-away gas accretion (Pollack et al. 1996). The hydrostatic gas accretion phase

starts when the embryo reaches a critical core mass ($\sim 10\,M_\oplus$, Mizuno 1980, Stevenson 1982). This phase can take up to $\sim 10\,$Myr and is the most time-consuming step in this classical core accretion model. The run-away gas accretion is triggered once the envelope and the core have comparable masses, and it sufficiently pushes the total mass to the giant planet regime ($\gtrsim 100\,M_\oplus$). In the inner region, embryos grow slowly and never reach the critical core mass before the gaseous disk is depleted. The later evolution involves collisions between these embryos in the gas-free environment. This so-called giant impact phase lasts $\sim 100\,$Myr and eventually forms the terrestrial planets (e.g., Chambers 2001).

A new paradigm that has attracted much attention recent years is pebble accretion. In the astrophysical context, pebbles are dust particles that are weakly coupled to the gas and thus drift in the disk. The inclusion of pebbles in the formation diagram provides a plausible scenario for the formation of planetesimals via streaming instability (Youdin & Goodman 2005, Johansen et al. 2007, Chiang & Youdin 2010). Unlike planetesimals that are decoupled from the gas, pebbles "feel" the aerodynamic drag from the gas and drift inward toward the star (Nakagawa et al. 1986). This means that the "food" supply to a protoplanet is not limited to the local material. Additionally, the cross-section for protoplanets (or planetesimals) to accrete pebbles is larger than the cross-section for the same objects to accrete planetesimals (Ormel & Klahr 2010, Lambrechts & Johansen 2012). These two factors together make pebble accretion more efficient in building up cores of protoplanets. When the protoplanet becomes massive enough, it starts to carve a gap in the pebble disk, and the subsequent pressure bump outside of the orbit stops the inward drifting pebbles. The corresponding mass of the protoplanet is called the pebble isolation mass

$$M_{\rm iso} \approx 10 \left(\frac{h/r}{0.04}\right)^3 M_\oplus \ , \qquad 24.$$

where h/r is the disk aspect ratio at location r and the prefactor is determined numerically and depends on disk properties (Lambrechts et al. 2014). The above relation assumes a solar-mass host star. For other stellar masses, the pebble isolation mass scales linearly with the mass of the host star (Liu et al. 2019). Once a protoplanet reaches the pebble isolation mass, it effectively cuts off the pebble flux and "starves" the protoplanetary core and all embryos interior to its orbit. With the halted pebble accretion, the critical core mass required to trigger the rapid gas accretion is reduced and thus giant planets can form more efficiently (Lambrechts et al. 2014). Furthermore, pebbles can easily vaporize in the hot envelopes before they can reach the cores (Brouwers et al. 2018). The enriched envelopes also speed up the formation of giant planets (Venturini et al. 2016; see also Stevenson 1982 and Hori & Ikoma 2011 for a similar mechanism in the planetesimal accretion scenario). We refer interested readers to the reviews by Johansen & Lambrechts (2017) and Ormel (2017) for more details about the pebble accretion model.

Planets may undergo disk-driven migration while accreting pebbles, planetesimals, and/or gas (e.g., Kley & Nelson 2012 and references therein). Migration can substantially change the architecture of the planetary system, such as locking planets into mean motion resonances (Goldreich & Tremaine 1980, Lee & Peale 2002). However, such features are not prominent in *Kepler* systems (see Section 2.4.2). This may suggest that most *Kepler* planets have not undergone significant disk-driven migrations (see also Section 4.2). Alternatively, the *Kepler* planets may have never entered into resonances during the migration (e.g., Goldreich & Schlichting 2014), or the long-term dynamical evolution after the disk dispersal has effectively removed most of these features (e.g., Izidoro et al. 2017, 2019).

4.2. Constraints from observations

Given the substantial uncertainties in theories and in some parts of observations, we think that it is premature to provide detailed and quantitative comparisons between theories and observations (but see attempts by, e.g., Hansen & Murray 2013, Izidoro et al. 2017, Mulders et al. 2019, Emsenhuber et al. 2020). We therefore choose to focus on some selected constraints that are considered relatively robust and discuss their implications to the formation of *Kepler*-like planets:

- **Prevalence and multiplicity.** Inner super Earth-like planets are known to exist around $\sim 30\%$ Sun-like stars, and they typically reside in multi-planet systems (Section 2.2). Additionally, they preferentially have outer cold Jupiter companions (Section 3.2), suggesting that the two types of planets do not inhibit, but perhaps promote, the formation of each other. Unlike giant planets, super Earths show a much weaker dependence on the host metallicity (Section 2.5.2).
- **Composition.** As inferred from population-level studies of the radius valley (Section 2.1.4) as well as mass and radii measurements of individual *Kepler* planets (e.g., Wu & Lithwick 2013, Hadden & Lithwick 2014, 2017), some inner small planets likely have Earth-like (i.e., rocky and ice-poor) cores, and these cores have acquired gaseous envelopes that weigh up to a few percent of the total mass while the disk is still present.

The prevalence and the early formation of super Earth-like planets suggest that the planet formation process is more efficient than what had been expected from solar system formation models (e.g., Ida & Lin 2004a, Mordasini et al. 2009). This alone may not be an issue to the pebble accretion scenario (see Section 4.1).[14] In fact, pebble accretion can be so efficient that preventing super Earth-mass planets from undergoing run-away gas accretion places another challenge, a possible solution to which could be a delayed formation near the end of the disk phase (e.g., Lee et al. 2014). For the planetesimal accretion scenario, a very massive disk is typically required to form super Earths efficiently and early (e.g., Emsenhuber et al. 2020). The rocky composition suggests that the cores are formed in the ice-poor environment, likely inside the water ice line. In order for embryos or protoplanets from outside of the ice line to not largely contaminate the inner region, the disk-driven migration is probably suppressed.

The strong correlation between inner super Earths and outer cold Jupiters is a bit challenging to both accretion scenarios under the typical protoplanetary disk conditions. The planetesimal accretion scenario usually requires relatively efficient disk-driven migrations to explain the presence of abundant super Earths around metal-poor hosts, but the same migration efficiency turns out an overkill in reproducing the inner–outer strong correlation (Schlecker et al. 2020, see also Ida & Lin 2010). For the pebble accretion scenario, because the solid supply to protoplanets is not limited locally, there is potentially a direct competition between different embryos. Furthermore, once the core of the outer giant planet first reaches the pebble isolation mass, the further growth of the inner planets is significantly limited, and the giant planet also acts as a barrier to the inward migrating embryos from outside of its orbit. Therefore, the pebble accretion scenario typically expects an

[14] Pebble accretion is efficient in growing planet embryos into larger bodies. However, pebble accretion is also lossy, as $\gtrsim 90\%$ of the planet-forming material falls onto the host star rather than being accreted onto the growing planets (Liu & Ormel 2018, Lin et al. 2018)

anti-correlation between inner and outer planets (Morbidelli et al. 2015, Izidoro et al. 2015, Lambrechts et al. 2019). Alternatively, the cores of both inner super Earths and outer cold Jupiters could be formed at such large separations (tens of AU) that enough material is available to the inner cores (Bitsch et al. 2015, 2019), although it is unclear whether such an approach can reproduce quantitatively the observed correlation and forms rocky core planets. The difficulty in reproducing the inner–outer correlation may suggest that many protoplanetary disks start heavier than what has been typically assumed. Indeed, if *Kepler* planets are formed *in situ* based on the local material (i.e., not the inward-drifting pebbles), the required surface density is much higher than the minimum-mass solar nebula model (Weidenschilling 1977, Hayashi 1981) and almost reaches the gravitational instability limit (Chiang & Laughlin 2013, Schlichting 2014).

5. SUMMARY AND DISCUSSION

The discovery of thousands of exoplanets from the combination of multiple detection techniques have substantially advanced our understanding of the distribution of planets and the architecture of planetary systems. This review aims to update our knowledge of exoplanet statistics since the Winn & Fabrycky (2015) review. In Section 2, we described the distribution and properties of planets in the inner region, based mostly on discoveries from the *Kepler* mission. In Section 3, we reviewed the recent progress on the cold planet population, with an emphasis on their connections to the close-in companions. Section 4 briefly described the theoretical models and the key constraints from observations. We summarize the key results below:

SUMMARY POINTS

1. In the inner region ($\lesssim 1\,\mathrm{AU}$), about 30% of Sun-like stars host planets with masses/radii down to Earth mass/radii, and each planetary system on average has about three such planets. These suggest that the planet formation process is more efficient than what had been expected from solar system formation models.
2. Planetary systems with more planets appear colder dynamically, with smaller orbital eccentricities, mutual inclinations, and orbital spacings. For systems with few planets in the inner region, planets can have ~ 0.3 orbital eccentricities and $\gtrsim 10^\circ$ mutual inclinations. These support the idea that dynamical evolution has played a significant role reshaping the system architecture.
3. There exists a "radius valley" at $R_\mathrm{p} \sim 2\,R_\oplus$ and $P \lesssim 30\,\mathrm{days}$. The valley was predicted by the photoevaporation theory, although alternative explanations have also been proposed. Population-level analyses of the radius valley suggest that these planets were probably born with rocky cores and gaseous atmospheres up to a few percent of the core masses.
4. Cold Neptune-like planets are a few times more abundant than cold Jupiter-like ones in the outer region. The inner ($\lesssim 1\,\mathrm{AU}$) and the outer ($\sim$1–10 AU) planetary systems appear strongly correlated such that inner small planets preferentially have cold Jupiter-like companions and that outer cold Jupiters almost always have inner planetary companions.

With the ongoing and upcoming missions that have better capabilities and/or open

up new observational channels, our understanding of exoplanets and planetary systems will continue to be improved. We outline below several promising directions that may see substantial advancement in the near future:

FUTURE PROSPECTS

1. Exoplanet atmosphere and mass–radius relation: Space-based all-sky transit surveys like the TESS mission (Ricker et al. 2015) have been finding many bright targets, enabling detailed characterizations of more close-in planets (e.g., Huang et al. 2018, Armstrong et al. 2020). An improved mass–radius relation and better atmospheric characterizations will help to understand the composition and potentially the past evolution of the planet (see the recent review by Madhusudhan 2019)
2. Planetary system architecture: The joint coverage of different surveys will potentially open up a larger parameter space (see **Figure 1**) and reveal more interesting features about the planetary system architecture. The *Gaia* mission alone is expected to detect at least thousands of giant planets around nearby stars (Perryman et al. 2014), and its synergy with other surveys/missions will also open up new channels into the architecture study (e.g., Xuan & Wyatt 2020, Damasso et al. 2020, De Rosa et al. 2020). RV follow-ups of systems detected by other methods could also play increasingly indispensable roles in this aspect, in particular with the extreme RV instruments with capability down to $\sim 0.3\,\mathrm{m\,s^{-1}}$ now coming online (e.g., Fischer et al. 2016).
3. Planet across the HR diagram: Rapid advances of large-scale spectroscopic surveys and the *Gaia* satellite are continuing to revolutionize stellar astrophysics and Galactic astronomy. Further synergies of large samples of exoplanets with detailed stellar chemical compositions, kinematics and/or ages measurements are expected to place planet formation in the rich context of stellar populations and evolutions.
4. Planets around young stars: While the present review focused on the planetary systems around $\gtrsim$Gyr old stars, the demographics of planets around young ($\lesssim$ 100 Myr) stars is a crucial link toward a more direct comparison with both planet formation theories and ALMA observations of protoplanetary disks (see the recent review by Andrews 2020). The detection and characterization of more planets around young stars (e.g., PDS 70b, c, Haffert et al. 2019 and AU Microscopii b, Plavchan et al. 2020) will be valuable.

DISCLOSURE STATEMENT

The authors are not aware of any affiliations, memberships, funding, or financial holdings that might be perceived as affecting the objectivity of this review.

ACKNOWLEDGMENTS

We thank Scott Gaudi, Andy Gould, Kento Masuda, Shude Mao, Chris Ormel, Scott Tremaine, and Josh Winn for comments and suggestions on the manuscript. SD was supported by the National Key R&D Program of China No. 2019YFA0405100. WZ was supported by the Natural Sciences and Engineering Research Council of Canada (NSERC)

under the funding reference #CITA 490888-16.

LITERATURE CITED

Adibekyan VZ, Sousa SG, Santos NC, Delgado Mena E, González Hernández JI, et al. 2012. A&A 545:A32
Agol E, Steffen J, Sari R, Clarkson W. 2005. MNRAS 359:567–579
Akeson RL, Chen X, Ciardi D, Crane M, Good J, et al. 2013. PASP 125:989
Andrews SM. 2020. ARA&A 58:483–528
Andrews SM, Rosenfeld KA, Kraus AL, Wilner DJ. 2013. ApJ 771:129
Ansdell M, Williams JP, van der Marel N, Carpenter JM, Guidi G, et al. 2016. ApJ 828:46
Armstrong DJ, Lopez TA, Adibekyan V, Booth RA, Bryant EM, et al. 2020. Nature 583:39–42
Artymowicz P, Lubow SH. 1994. ApJ 421:651
Bailey E, Batygin K. 2018. ApJ 866:L2
Ballard S, Johnson JA. 2016. ApJ 816:66
Beaugé C, Nesvorný D. 2013. ApJ 763:12
Becker JC, Vanderburg A, Adams FC, Rappaport SA, Schwengeler HM. 2015. ApJ 812:L18
Bennett DP, Rhie SH. 1996. ApJ 472:660
Berger TA, Huber D, Gaidos E, van Saders JL. 2018. ApJ 866:99
Berger TA, Huber D, Gaidos E, van Saders JL, Weiss LM. 2020a. AJ 160:108
Berger TA, Huber D, van Saders JL, Gaidos E, Tayar J, Kraus AL. 2020b. AJ 159:280
Bitsch B, Izidoro A, Johansen A, Raymond SN, Morbidelli A, et al. 2019. A&A 623:A88
Bitsch B, Lambrechts M, Johansen A. 2015. A&A 582:A112
Borucki WJ, Koch D, Basri G, Batalha N, Brown T, et al. 2010. *Science* 327:977
Bouma LG, Masuda K, Winn JN. 2018. AJ 155:244
Bowler BP. 2016. PASP 128:102001
Brewer JM, Wang S, Fischer DA, Foreman-Mackey D. 2018. ApJ 867:L3
Brouwers MG, Vazan A, Ormel CW. 2018. A&A 611:A65
Bryan ML, Knutson HA, Howard AW, Ngo H, Batygin K, et al. 2016. ApJ 821:89
Bryan ML, Knutson HA, Lee EJ, Fulton BJ, Batygin K, et al. 2019. AJ 157:52
Buchhave LA, Bitsch B, Johansen A, Latham DW, Bizzarro M, et al. 2018. ApJ 856:37
Buchhave LA, Latham DW, Johansen A, Bizzarro M, Torres G, et al. 2012. Nature 486:375–377
Burke CJ, Catanzarite J. 2017a. Planet Detection Metrics: Per-Target Detection Contours for Data Release 25. Kepler Science Document KSCI-19111-002
Burke CJ, Catanzarite J. 2017b. Planet Detection Metrics: Per-Target Flux-Level Transit Injection Tests of TPS for Data Release 25. Kepler Science Document KSCI-19109-002
Burke CJ, Christiansen JL, Mullally F, Seader S, Huber D, et al. 2015. ApJ 809:8
Burt JA, Nielsen LD, Quinn SN, Mamajek EE, Matthews EC, et al. 2020. AJ 160:153
Cañas CI, Wang S, Mahadevan S, Bender CF, De Lee N, et al. 2019. ApJ 870:L17
Cassan A, Kubas D, Beaulieu JP, Dominik M, Horne K, et al. 2012. Nature 481:167–169
Chamberlin TC. 1916. JRASC 10:473
Chambers JE. 2001. Icarus 152:205–224
Chambers JE, Wetherill GW, Boss AP. 1996. Icarus 119:261–268
Chaplin WJ, Miglio A. 2013. ARA&A 51:353–392
Chatterjee S, Ford EB, Matsumura S, Rasio FA. 2008. ApJ 686:580–602
Chen J, Kipping D. 2017. ApJ 834:17
Chiang E, Laughlin G. 2013. MNRAS 431:3444–3455
Chiang E, Youdin AN. 2010. *Annual Review of Earth and Planetary Sciences* 38:493–522
Christiansen JL, Clarke BD, Burke CJ, Jenkins JM, Bryson ST, et al. 2020. AJ 160:159
Christiansen JL, Clarke BD, Burke CJ, Seader S, Jenkins JM, et al. 2015. ApJ 810:95
Ciardi DR, Beichman CA, Horch EP, Howell SB. 2015. ApJ 805:16

Ciardi DR, Fabrycky DC, Ford EB, Gautier T. N. I, Howell SB, et al. 2013. ApJ 763:41
Clanton C, Gaudi BS. 2014. ApJ 791:91
Clanton C, Gaudi BS. 2016. ApJ 819:125
Cumming A, Butler RP, Marcy GW, Vogt SS, Wright JT, Fischer DA. 2008. PASP 120:531
Dai F, Masuda K, Winn JN. 2018. ApJ 864:L38
Damasso M, Sozzetti A, Lovis C, Barros SCC, Sousa SG, et al. 2020. A&A 642:A31
Dawson RI, Chiang E. 2014. *Science* 346:212–216
Dawson RI, Johnson JA. 2018. ARA&A 56:175–221
Dawson RI, Murray-Clay RA. 2013. ApJ 767:L24
De Cat P, Fu JN, Ren AB, Yang XH, Shi JR, et al. 2015. ApJS 220:19
De Rosa RJ, Dawson R, Nielsen EL. 2020. A&A 640:A73
Deck KM, Payne M, Holman MJ. 2013. ApJ 774:129
Dong S, DePoy DL, Gaudi BS, Gould A, Han C, et al. 2006. ApJ 642:842–860
Dong S, Gould A, Udalski A, Anderson J, Christie GW, et al. 2009. ApJ 695:970–987
Dong S, Katz B, Socrates A. 2014a. ApJ 781:L5
Dong S, Xie JW, Zhou JL, Zheng Z, Luo A. 2018. *Proceedings of the National Academy of Science* 115:266–271
Dong S, Zheng Z, Zhu Z, De Cat P, Fu JN, et al. 2014b. ApJ 789:L3
Dong S, Zhu Z. 2013. ApJ 778:53
Dressing CD, Charbonneau D. 2013. ApJ 767:95
Dressing CD, Charbonneau D. 2015. ApJ 807:45
Duchêne G, Kraus A. 2013. ARA&A 51:269–310
Emsenhuber A, Mordasini C, Burn R, Alibert Y, Benz W, Asphaug E. 2020. *arXiv e-prints* :arXiv:2007.05562
Fabrycky DC, Lissauer JJ, Ragozzine D, Rowe JF, Steffen JH, et al. 2014. ApJ 790:146
Fang J, Margot JL. 2012. ApJ 761:92
Fang J, Margot JL. 2013. ApJ 767:115
Fernandes RB, Mulders GD, Pascucci I, Mordasini C, Emsenhuber A. 2019. ApJ 874:81
Figueira P, Marmier M, Boué G, Lovis C, Santos NC, et al. 2012. A&A 541:A139
Fischer DA, Anglada-Escude G, Arriagada P, Baluev RV, Bean JL, et al. 2016. PASP 128:066001
Fischer DA, Valenti J. 2005. ApJ 622:1102–1117
Ford EB, Quinn SN, Veras D. 2008. ApJ 678:1407–1418
Ford EB, Rowe JF, Fabrycky DC, Carter JA, Holman MJ, et al. 2011. ApJS 197:2
Foreman-Mackey D, Hogg DW, Morton TD. 2014. ApJ 795:64
Foreman-Mackey D, Morton TD, Hogg DW, Agol E, Schölkopf B. 2016. AJ 152:206
Fressin F, Torres G, Charbonneau D, Bryson ST, Christiansen J, et al. 2013. ApJ 766:81
Fulton BJ, Petigura EA. 2018. AJ 156:264
Fulton BJ, Petigura EA, Howard AW, Isaacson H, Marcy GW, et al. 2017. AJ 154:109
Funk B, Wuchterl G, Schwarz R, Pilat-Lohinger E, Eggl S. 2010. A&A 516:A82
Furlan E, Ciardi DR, Everett ME, Saylors M, Teske JK, et al. 2017. AJ 153:71
Gaia Collaboration, Brown AGA, Vallenari A, Prusti T, de Bruijne JHJ, et al. 2018. A&A 616:A1
Gaia Collaboration, Prusti T, de Bruijne JHJ, Brown AGA, Vallenari A, et al. 2016. A&A 595:A1
Gandolfi D, Barragán O, Livingston JH, Fridlund M, Justesen AB, et al. 2018. A&A 619:L10
Gaudi BS. 2012. ARA&A 50:411–453
Gilbert GJ, Fabrycky DC. 2020. AJ 159:281
Ginzburg S, Schlichting HE, Sari R. 2018. MNRAS 476:759–765
Goldreich P, Schlichting HE. 2014. AJ 147:32
Goldreich P, Tremaine S. 1980. ApJ 241:425–441
Gould A. 2016. *Journal of Korean Astronomical Society* 49:123–126
Gould A, Dong S, Gaudi BS, Udalski A, Bond IA, et al. 2010. ApJ 720:1073–1089
Gould A, Dorsher S, Gaudi BS, Udalski A. 2006a. Acta Astron. 56:1–50

Gould A, Loeb A. 1992. ApJ 396:104

Gould A, Ryu YH, Calchi Novati S, Zang W, Albrow MD, et al. 2020a. *Journal of Korean Astronomical Society* 53:9–26

Gould A, Udalski A, An D, Bennett DP, Zhou AY, et al. 2006b. ApJ 644:L37–L40

Gould A, Zang W, Mao S, Dong S. 2020b. *arXiv e-prints* :arXiv:2010.09671

Guo X, Johnson JA, Mann AW, Kraus AL, Curtis JL, Latham DW. 2017. ApJ 838:25

Gupta A, Schlichting HE. 2019. MNRAS 487:24–33

Gupta A, Schlichting HE. 2020. MNRAS 493:792–806

Hadden S, Lithwick Y. 2014. ApJ 787:80

Hadden S, Lithwick Y. 2017. AJ 154:5

Hadden S, Lithwick Y. 2018. AJ 156:95

Haffert SY, Bohn AJ, de Boer J, Snellen IAG, Brinchmann J, et al. 2019. *Nature Astronomy* 3:749–754

Hallatt T, Lee EJ. 2020. ApJ 904:134

Hamer JH, Schlaufman KC. 2020. AJ 160:138

Han C, Gaudi BS, An JH, Gould A. 2005. ApJ 618:962–972

Hansen BMS, Murray N. 2013. ApJ 775:53

Hayashi C. 1981. *Progress of Theoretical Physics Supplement* 70:35–53

He MY, Ford EB, Ragozzine D. 2019. MNRAS 490:4575–4605

He MY, Ford EB, Ragozzine D, Carrera D. 2020. AJ 160:276

Herman MK, Zhu W, Wu Y. 2019. AJ 157:248

Hirano T, Dai F, Gandolfi D, Fukui A, Livingston JH, et al. 2018. AJ 155:127

Hoffman Kelsey L, Rowe JF. 2017. Uniform Modeling of KOIs: MCMC Notes for Data Release 25. Kepler Science Document KSCI-19113-001

Holczer T, Mazeh T, Nachmani G, Jontof-Hutter D, Ford EB, et al. 2016. ApJS 225:9

Holman MJ, Murray NW. 2005. *Science* 307:1288–1291

Holman MJ, Wiegert PA. 1999. AJ 117:621–628

Hori Y, Ikoma M. 2011. MNRAS 416:1419–1429

Howard AW, Marcy GW, Bryson ST, Jenkins JM, Rowe JF, et al. 2012. ApJS 201:15

Hsu DC, Ford EB, Ragozzine D, Ashby K. 2019. AJ 158:109

Hsu DC, Ford EB, Ragozzine D, Morehead RC. 2018. AJ 155:205

Huang C, Wu Y, Triaud AHMJ. 2016. ApJ 825:98

Huang CX, Burt J, Vanderburg A, Günther MN, Shporer A, et al. 2018. ApJ 868:L39

Huang CX, Petrovich C, Deibert E. 2017. AJ 153:210

Huang CX, Quinn SN, Vanderburg A, Becker J, Rodriguez JE, et al. 2020. ApJ 892:L7

Ida S, Kokubo E, Makino J. 1993. MNRAS 263:875

Ida S, Lin DNC. 2004a. ApJ 604:388–413

Ida S, Lin DNC. 2004b. ApJ 616:567–572

Ida S, Lin DNC. 2010. ApJ 719:810–830

Ida S, Lin DNC, Nagasawa M. 2013. ApJ 775:42

Ida S, Makino J. 1993. Icarus 106:210–227

Izidoro A, Bitsch B, Raymond SN, Johansen A, Morbidelli A, et al. 2019. *arXiv e-prints* :arXiv:1902.08772

Izidoro A, Ogihara M, Raymond SN, Morbidelli A, Pierens A, et al. 2017. MNRAS 470:1750–1770

Izidoro A, Raymond SN, Morbidelli Ar, Hersant F, Pierens A. 2015. ApJ 800:L22

Jackson AP, Davis TA, Wheatley PJ. 2012. MNRAS 422:2024–2043

Jackson B, Stark CC, Adams ER, Chambers J, Deming D. 2013. ApJ 779:165

Jiang CF, Xie JW, Zhou JL. 2020. AJ 160:180

Jin S, Mordasini C. 2018. ApJ 853:163

Johansen A, Davies MB, Church RP, Holmelin V. 2012. ApJ 758:39

Johansen A, Lambrechts M. 2017. *Annual Review of Earth and Planetary Sciences* 45:359–387

Johansen A, Oishi JS, Mac Low MM, Klahr H, Henning T, Youdin A. 2007. Nature 448:1022–1025
Johnson JA, Aller KM, Howard AW, Crepp JR. 2010. PASP 122:905
Johnson JA, Butler RP, Marcy GW, Fischer DA, Vogt SS, et al. 2007. ApJ 670:833–840
Johnson JA, Petigura EA, Fulton BJ, Marcy GW, Howard AW, et al. 2017. AJ 154:108
Johnson SA, Penny M, Gaudi BS, Kerins E, Rattenbury NJ, et al. 2020. AJ 160:123
Jung YK, Gould A, Zang W, Hwang KH, Ryu YH, et al. 2019. AJ 157:72
Jurić M, Tremaine S. 2008. ApJ 686:603–620
Kane SR, Ciardi DR, Gelino DM, von Braun K. 2012. MNRAS 425:757–762
Kawahara H, Masuda K. 2019. AJ 157:218
Kennedy GM, Kenyon SJ. 2008. ApJ 673:502–512
Kim HW, Hwang KH, Gould A, Yee JC, Ryu YH, et al. 2020. *arXiv e-prints* :arXiv:2007.06870
Kim SL, Lee CU, Park BG, Kim DJ, Cha SM, et al. 2016. *Journal of Korean Astronomical Society* 49:37–44
King GW, Wheatley PJ. 2021. MNRAS 501:L28–L32
Kipping D. 2018. MNRAS 473:784–795
Kley W, Nelson RP. 2012. ARA&A 50:211–249
Knutson HA, Fulton BJ, Montet BT, Kao M, Ngo H, et al. 2014. ApJ 785:126
Kokubo E, Ida S. 1998. Icarus 131:171–178
Kraus AL, Ireland MJ, Huber D, Mann AW, Dupuy TJ. 2016. AJ 152:8
Kruijer TS, Burkhardt C, Budde G, Kleine T. 2017. *Proceedings of the National Academy of Science* 114:6712–6716
Kurokawa H, Nakamoto T. 2014. ApJ 783:54
Kutra T, Wu Y. 2020. *arXiv e-prints* :arXiv:2003.08431
Lambrechts M, Johansen A. 2012. A&A 544:A32
Lambrechts M, Johansen A, Morbidelli A. 2014. A&A 572:A35
Lambrechts M, Morbidelli A, Jacobson SA, Johansen A, Bitsch B, et al. 2019. A&A 627:A83
Laskar J. 1997. A&A 317:L75–L78
Laskar J, Petit AC. 2017. A&A 605:A72
Lee EJ. 2019. ApJ 878:36
Lee EJ, Chiang E. 2017. ApJ 842:40
Lee EJ, Chiang E, Ormel CW. 2014. ApJ 797:95
Lee EJ, Connors NJ. 2020. *arXiv e-prints* :arXiv:2008.01105
Lee MH, Peale SJ. 2002. ApJ 567:596–609
Limbach MA, Turner EL. 2015. *Proceedings of the National Academy of Science* 112:20–24
Lin DNC, Bodenheimer P, Richardson DC. 1996. Nature 380:606–607
Lin JW, Lee EJ, Chiang E. 2018. MNRAS 480:4338–4354
Lissauer JJ. 1993. ARA&A 31:129–174
Lissauer JJ, Ragozzine D, Fabrycky DC, Steffen JH, Ford EB, et al. 2011. ApJS 197:8
Lithwick Y, Xie J, Wu Y. 2012. ApJ 761:122
Liu B, Lambrechts M, Johansen A, Liu F. 2019. A&A 632:A7
Liu B, Ormel CW. 2018. A&A 615:A138
Liu F, Yong D, Asplund M, Ramírez I, Meléndez J, et al. 2016. MNRAS 456:2636–2646
Lloyd JP. 2011. ApJ 739:L49
Lopez ED, Fortney JJ. 2013. ApJ 776:2
Lopez ED, Rice K. 2018. MNRAS 479:5303–5311
Lundkvist MS, Kjeldsen H, Albrecht S, Davies GR, Basu S, et al. 2016. *Nature Communications* 7:11201
Ma S, Mao S, Ida S, Zhu W, Lin DNC. 2016. MNRAS 461:L107–L111
Madhusudhan N. 2019. ARA&A 57:617–663
Malla SP, Stello D, Huber D, Montet BT, Bedding TR, et al. 2020. MNRAS 496:5423–5435
Mao S. 2012. *Research in Astronomy and Astrophysics* 12:947–972

Mao S, Paczynski B. 1991. ApJ 374:L37
Masuda K, Winn JN, Kawahara H. 2020. AJ 159:38
Matsakos T, Königl A. 2016. ApJ 820:L8
Mayor M, Marmier M, Lovis C, Udry S, Ségransan D, et al. 2011. *arXiv e-prints* :arXiv:1109.2497
Mayor M, Queloz D. 1995. Nature 378:355–359
Mazeh T, Holczer T, Faigler S. 2016. A&A 589:A75
McArthur BE, Benedict GF, Barnes R, Martioli E, Korzennik S, et al. 2010. ApJ 715:1203–1220
McDonald GD, Kreidberg L, Lopez E. 2019. ApJ 876:22
Millholland S, Laughlin G. 2019. *Nature Astronomy* 3:424–433
Millholland S, Wang S, Laughlin G. 2017. ApJ 849:L33
Mills SM, Fabrycky DC. 2017. AJ 153:45
Mills SM, Howard AW, Petigura EA, Fulton BJ, Isaacson H, Weiss LM. 2019. AJ 157:198
Mizuno H. 1980. *Progress of Theoretical Physics* 64:544–557
Moe M, Kratter KM. 2019. *arXiv e-prints* :arXiv:1912.01699
Moe M, Kratter KM, Badenes C. 2019. ApJ 875:61
Moorhead AV, Ford EB, Morehead RC, Rowe J, Borucki WJ, et al. 2011. ApJS 197:1
Morbidelli A, Lambrechts M, Jacobson S, Bitsch B. 2015. Icarus 258:418–429
Mordasini C, Alibert Y, Benz W. 2009. A&A 501:1139–1160
Morton TD, Bryson ST, Coughlin JL, Rowe JF, Ravichandran G, et al. 2016. ApJ 822:86
Mróz P, Poleski R, Gould A, Udalski A, Sumi T, et al. 2020a. ApJ 903:L11
Mróz P, Poleski R, Han C, Udalski A, Gould A, et al. 2020b. AJ 159:262
Mróz P, Ryu YH, Skowron J, Udalski A, Gould A, et al. 2018. AJ 155:121
Mróz P, Udalski A, Bennett DP, Ryu YH, Sumi T, et al. 2019. A&A 622:A201
Mróz P, Udalski A, Skowron J, Poleski R, Kozłowski S, et al. 2017. Nature 548:183–186
Mulders GD, Mordasini C, Pascucci I, Ciesla FJ, Emsenhuber A, Apai D. 2019. ApJ 887:157
Mulders GD, Pascucci I, Apai D. 2015a. ApJ 798:112
Mulders GD, Pascucci I, Apai D. 2015b. ApJ 814:130
Mulders GD, Pascucci I, Apai D, Ciesla FJ. 2018. AJ 156:24
Mulders GD, Pascucci I, Apai D, Frasca A, Molenda-Żakowicz J. 2016. AJ 152:187
Munoz Romero CE, Kempton EMR. 2018. AJ 155:134
Murchikova L, Tremaine S. 2020. AJ 160:160
Nakagawa Y, Sekiya M, Hayashi C. 1986. Icarus 67:375–390
Ngo H, Knutson HA, Hinkley S, Bryan M, Crepp JR, et al. 2016. ApJ 827:8
Nielsen EL, De Rosa RJ, Macintosh B, Wang JJ, Ruffio JB, et al. 2019. AJ 158:13
Ofir A, Xie JW, Jiang CF, Sari R, Aharonson O. 2018. ApJS 234:9
Ormel CW. 2017. *The Emerging Paradigm of Pebble Accretion*, vol. 445 of *Astrophysics and Space Science Library*. 197
Ormel CW, Klahr HH. 2010. A&A 520:A43
Owen JE. 2019. *Annual Review of Earth and Planetary Sciences* 47:67–90
Owen JE, Lai D. 2018. MNRAS 479:5012–5021
Owen JE, Murray-Clay R. 2018. MNRAS 480:2206–2216
Owen JE, Wu Y. 2013. ApJ 775:105
Owen JE, Wu Y. 2017. ApJ 847:29
Pascucci I, Mulders GD, Gould A, Fernand es R. 2018. ApJ 856:L28
Penny MT, Gaudi BS, Kerins E, Rattenbury NJ, Mao S, et al. 2019. ApJS 241:3
Perryman M, Hartman J, Bakos GÁ, Lindegren L. 2014. ApJ 797:14
Petigura EA, Howard AW, Marcy GW. 2013. *Proceedings of the National Academy of Science* 110:19273–19278
Petigura EA, Howard AW, Marcy GW, Johnson JA, Isaacson H, et al. 2017. AJ 154:107
Petigura EA, Marcy GW, Winn JN, Weiss LM, Fulton BJ, et al. 2018. AJ 155:89
Petrovich C, Deibert E, Wu Y. 2019. AJ 157:180

Petrovich C, Tremaine S. 2016. ApJ 829:132
Plavchan P, Barclay T, Gagné J, Gao P, Cale B, et al. 2020. Nature 582:497–500
Plavchan P, Bilinski C, Currie T. 2014. PASP 126:34
Poleski R, Skowron J, Udalski A, Han C, Kozłowski S, et al. 2014. ApJ 795:42
Pollack JB, Hubickyj O, Bodenheimer P, Lissauer JJ, Podolak M, Greenzweig Y. 1996. Icarus 124:62–85
Pu B, Lai D. 2019. MNRAS 488:3568–3587
Pu B, Lai D. 2020. *arXiv e-prints* :arXiv:2008.05698
Pu B, Wu Y. 2015. ApJ 807:44
Quillen AC. 2011. MNRAS 418:1043–1054
Rasio FA, Ford EB. 1996a. *Science* 274:954–956
Rasio FA, Ford EB. 1996b. *Science* 274:954–956
Raymond SN, Barnes R, Mandell AM. 2008. MNRAS 384:663–674
Ricker GR, Winn JN, Vanderspek R, Latham DW, Bakos GÁ, et al. 2015. *Journal of Astronomical Telescopes, Instruments, and Systems* 1:014003
Rogers JG, Owen JE. 2020. *arXiv e-prints* :arXiv:2007.11006
Ryu YH, Mróz P, Gould A, Hwang KH, Kim HW, et al. 2020. *arXiv e-prints* :arXiv:2010.07527
Safronov VS. 1972. *Evolution of the protoplanetary cloud and formation of the earth and planets.*
Sanchis-Ojeda R, Rappaport S, Winn JN, Kotson MC, Levine A, El Mellah I. 2014. ApJ 787:47
Sandford E, Kipping D, Collins M. 2019. MNRAS 489:3162–3173
Santerne A, Moutou C, Tsantaki M, Bouchy F, Hébrard G, et al. 2016. A&A 587:A64
Santos NC, Israelian G, Mayor M. 2001. A&A 373:1019–1031
Schlaufman KC, Lin DNC, Ida S. 2010. ApJ 724:L53–L58
Schlaufman KC, Winn JN. 2013. ApJ 772:143
Schlaufman KC, Winn JN. 2016. ApJ 825:62
Schlecker M, Mordasini C, Emsenhuber A, Klahr H, Henning T, et al. 2020. *arXiv e-prints* :arXiv:2007.05563
Schlichting HE. 2014. ApJ 795:L15
Seager S, Mallén-Ornelas G. 2003. ApJ 585:1038–1055
Shallue CJ, Vanderburg A. 2018. AJ 155:94
Skidmore W, TMT International Science Development Teams, Science Advisory Committee T. 2015. *Research in Astronomy and Astrophysics* 15:1945
Sousa SG, Santos NC, Mayor M, Udry S, Casagrande L, et al. 2008. A&A 487:373–381
Steffen JH, Batalha NM, Borucki WJ, Buchhave LA, Caldwell DA, et al. 2010. ApJ 725:1226–1241
Steffen JH, Farr WM. 2013. ApJ 774:L12
Steffen JH, Ragozzine D, Fabrycky DC, Carter JA, Ford EB, et al. 2012. *Proceedings of the National Academy of Science* 109:7982–7987
Stevenson DJ. 1982. Planet. Space Sci. 30:755–764
Sumi T, Bennett DP, Bond IA, Udalski A, Batista V, et al. 2010. ApJ 710:1641–1653
Sumi T, Kamiya K, Bennett DP, Bond IA, Abe F, et al. 2011. Nature 473:349–352
Suzuki D, Bennett DP, Ida S, Mordasini C, Bhattacharya A, et al. 2018. ApJ 869:L34
Suzuki D, Bennett DP, Sumi T, Bond IA, Rogers LA, et al. 2016. ApJ 833:145
Szabó GM, Kiss LL. 2011. ApJ 727:L44
Tabachnik S, Tremaine S. 2002. MNRAS 335:151–158
Terquem C, Papaloizou JCB. 2019. MNRAS 482:530–549
Teske J, Díaz MR, Luque R, Močnik T, Seidel JV, et al. 2020. AJ 160:96
Teske JK, Thorngren D, Fortney JJ, Hinkel N, Brewer JM. 2019. AJ 158:239
Thompson SE, Coughlin JL, Hoffman K, Mullally F, Christiansen JL, et al. 2018. ApJS 235:38
Tremaine S. 2015. ApJ 807:157
Tremaine S, Dong S. 2012. AJ 143:94
Tu L, Johnstone CP, Güdel M, Lammer H. 2015. A&A 577:L3

Udalski A, Ryu YH, Sajadian S, Gould A, Mróz P, et al. 2018. Acta Astron. 68:1–42
Uehara S, Kawahara H, Masuda K, Yamada S, Aizawa M. 2016. ApJ 822:2
Van Eylen V, Agentoft C, Lundkvist MS, Kjeldsen H, Owen JE, et al. 2018. MNRAS 479:4786–4795
Van Eylen V, Albrecht S. 2015. ApJ 808:126
Van Eylen V, Albrecht S, Huang X, MacDonald MG, Dawson RI, et al. 2019. AJ 157:61
Venturini J, Alibert Y, Benz W. 2016. A&A 596:A90
Wang J, Fischer DA. 2015. AJ 149:14
Wang J, Fischer DA, Xie JW, Ciardi DR. 2015. ApJ 813:130
Wang J, Xie JW, Barclay T, Fischer DA. 2014. ApJ 783:4
Weidenschilling SJ. 1977. Ap&SS 51:153–158
Weidenschilling SJ, Marzari F. 1996. Nature 384:619–621
Weiss LM, Isaacson HT, Marcy GW, Howard AW, Petigura EA, et al. 2018a. AJ 156:254
Weiss LM, Marcy GW, Petigura EA, Fulton BJ, Howard AW, et al. 2018b. AJ 155:48
Weiss LM, Petigura EA. 2020. ApJ 893:L1
Winn JN. 2010. *arXiv e-prints* :arXiv:1001.2010
Winn JN, Fabrycky DC. 2015. ARA&A 53:409–447
Winn JN, Sanchis-Ojeda R, Rappaport S. 2018. New A Rev. 83:37–48
Winn JN, Sanchis-Ojeda R, Rogers L, Petigura EA, Howard AW, et al. 2017. AJ 154:60
Wisdom J. 1980. AJ 85:1122–1133
Wittenmyer RA, Butler RP, Tinney CG, Horner J, Carter BD, et al. 2016. ApJ 819:28
Woolfson MM. 1993. QJRAS 34:1–20
Wright JT, Marcy GW, Howard AW, Johnson JA, Morton TD, Fischer DA. 2012. ApJ 753:160
Wright JT, Upadhyay S, Marcy GW, Fischer DA, Ford EB, Johnson JA. 2009. ApJ 693:1084–1099
Wright JT, Veras D, Ford EB, Johnson JA, Marcy GW, et al. 2011. ApJ 730:93
Wu Y. 2019. ApJ 874:91
Wu Y, Lithwick Y. 2013. ApJ 772:74
Xie JW, Dong S, Zhu Z, Huber D, Zheng Z, et al. 2016. *Proceedings of the National Academy of Science* 113:11431–11435
Xie JW, Wu Y, Lithwick Y. 2014. ApJ 789:165
Xuan JW, Wyatt MC. 2020. MNRAS
Yalinewich A, Petrovich C. 2020. ApJ 892:L11
Yang JY, Xie JW, Zhou JL. 2020. AJ 159:164
Yee JC, Zang W, Udalski A, Ryu YH, Green J, et al. 2021. *arXiv e-prints* :arXiv:2101.04696
Youdin AN. 2011. ApJ 742:38
Youdin AN, Goodman J. 2005. ApJ 620:459–469
Zang W, Han C, Kondo I, Yee JC, Lee CU, et al. 2021. *arXiv e-prints* :arXiv:2103.01896
Zapatero Osorio MR, Béjar VJS, Martín EL, Rebolo R, Barrado y Navascués D, et al. 2000. *Science* 290:103–107
Zhou JL, Lin DNC, Sun YS. 2007. ApJ 666:423–435
Zhu W. 2019. ApJ 873:8
Zhu W. 2020. AJ 159:188
Zhu W, Dai F, Masuda K. 2018a. *Research Notes of the American Astronomical Society* 2:160
Zhu W, Petrovich C, Wu Y, Dong S, Xie J. 2018b. ApJ 860:101
Zhu W, Wang J, Huang C. 2016. ApJ 832:196
Zhu W, Wu Y. 2018. AJ 156:92
Ziegler C, Law NM, Baranec C, Riddle R, Duev DA, et al. 2018. AJ 155:161
Zink JK, Christiansen JL, Hansen BMS. 2019. MNRAS 483:4479–4494
Zinzi A, Turrini D. 2017. A&A 605:L4
Zong W, Fu JN, De Cat P, Shi J, Luo A, et al. 2018. ApJS 238:30